Supplementary Information for

Regulation of H^+ transfer pathways promotes C-C coupling in acidic CO_2 electroreduction

Qi Jin[1,†], Yun Yang[1,†], Dongao Zhang[1], Xiaodong Yi[1,*], Guoxiong Wang[2,3,*], and Zhou Chen[1,*]

[1] College of Materials, College of Chemistry and Chemical Engineering, State Key Laboratory for Physical Chemistry of Solid Surfaces, Xiamen University, Xiamen 361005, China.

[2] Advanced Institute for Future Energy, Shanghai Key Laboratory of Electrochemical and Thermochemical Conversion for Resources Recycling, State Key Laboratory of Porous Materials for Separation and Conversion, iChEM (Collaborative Innovation Center of Chemistry for Energy Materials), Department of Chemistry, Fudan University, Shanghai 200438, China.

[3] State Key Laboratory of Catalysis, Dalian National Laboratory for Clean Energy, iChEM (Collaborative Innovation Center of Chemistry for Energy Materials), Dalian Institute of Chemical Physics, Chinese Academy of Sciences, Dalian 116023, China.

[†] These authors contributed equally.

* Corresponding authors.

E-mail addresses: xdyi@xmu.edu.cn (X. Yi); wangguoxiong@fudan.edu.cn (G. Wang); zhouchen@xmu.edu.cn (Z. Chen).

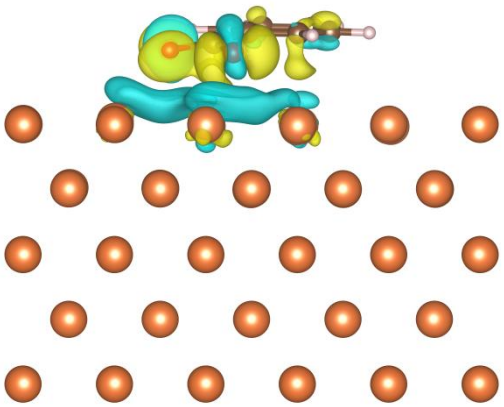

Supplementary Figure 1. Charge density difference analysis and Bader charge analysis of benzoic acid (BZA)-Cu(100). Yellow represents charge accumulation, and blue represents charge dissipation.

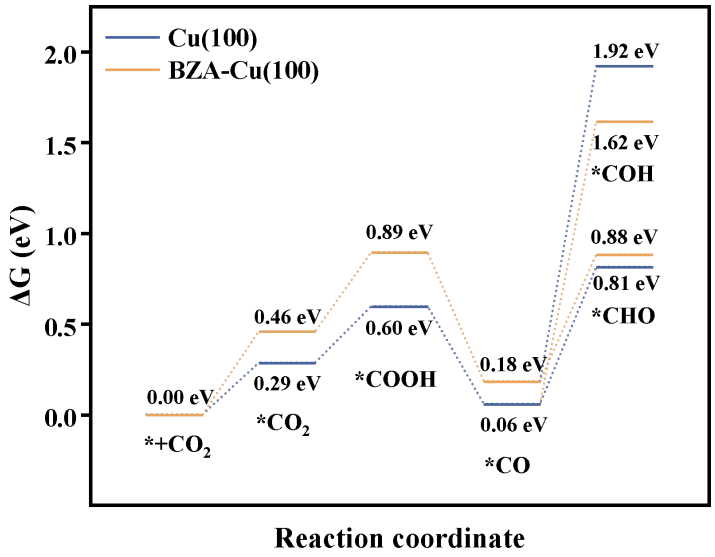

Supplementary Figure 2. Free energy diagrams of CO_2 hydrogenation and CO hydrogenation via different pathways on Cu(100) and BZA-Cu(100) surfaces.

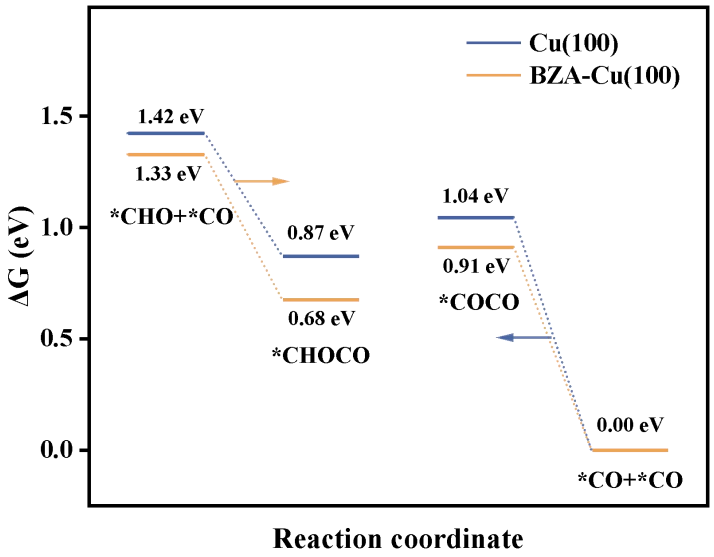

Supplementary Figure 3. Free energy diagrams of the coupling of two pathways on Cu(100) and BZA-Cu(100) surfaces.

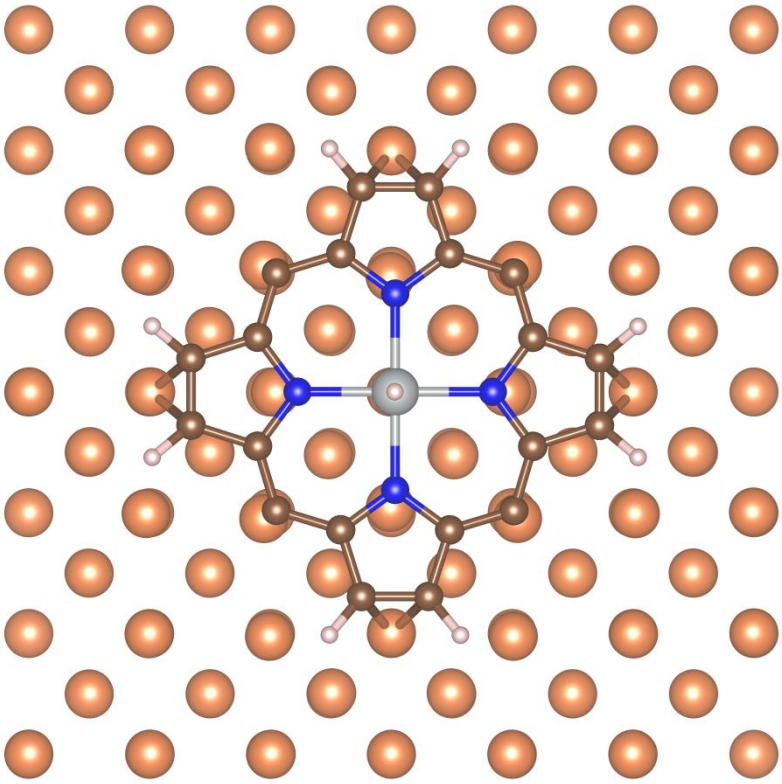

Supplementary Figure 4. Schematic diagram of the modified metalloporphyrin ring model on Cu(100) surface, where gray represents metal M (M = Ag, Co, Ni, Cu, Au, Pd, Pt, Zn, and Mg).

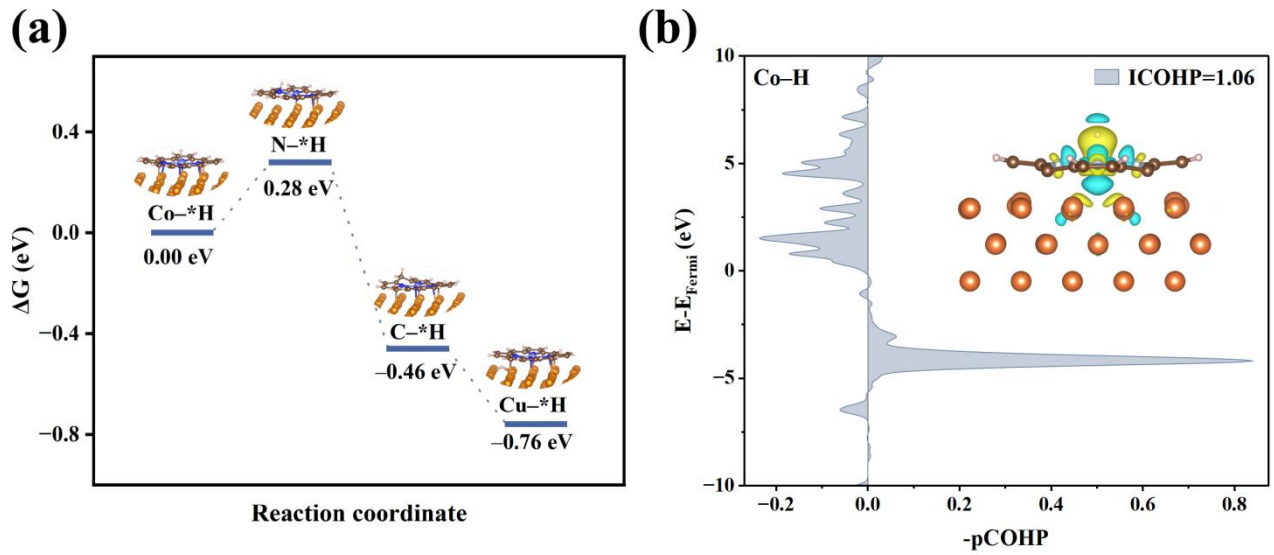

Supplementary Figure 5. (a) Free energy profile for the hydrogen spillover pathway. (b) The Crystal Orbital Hamilton Population (-pCOHP) and ICOHP profiles for the Co–H bond; and side views of the charge density difference for the Co–porphyrin–H configuration. Yellow and cyan isosurfaces represent regions of electron accumulation and depletion, respectively.

Supplementary Note 1: The free energy step diagram depicts a plausible hydrogen spillover pathway, illustrating the sequential migration of the adsorbed H species from the Co center to an adjacent pyrrolic N atom, subsequently to a C atom of the porphyrin ring, and ultimately onto the Cu substrate. This step-wise energetic analysis demonstrates the thermodynamic feasibility of the H spillover process.

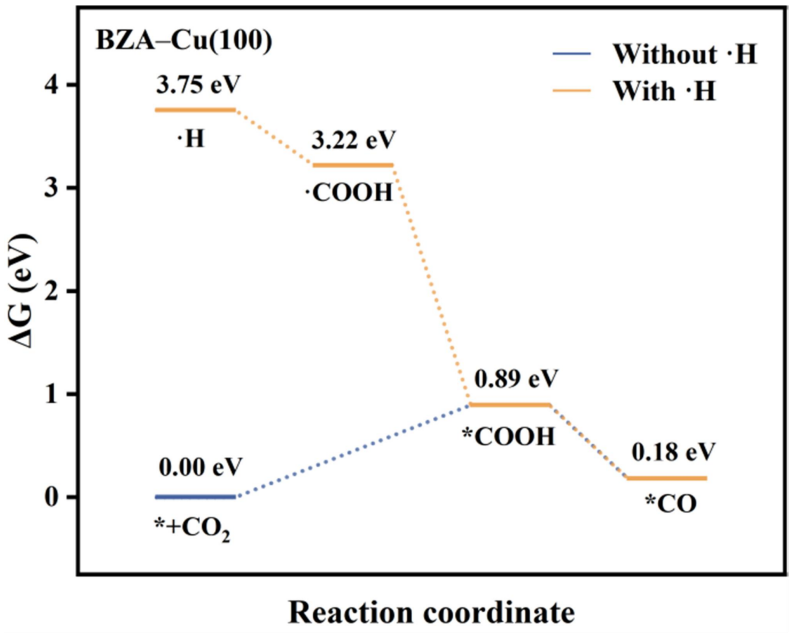

Supplementary Figure 6. Free energy diagrams of the CO_2 hydrogenation step with or without the involvement of ·H radical on BZA-Cu(100).

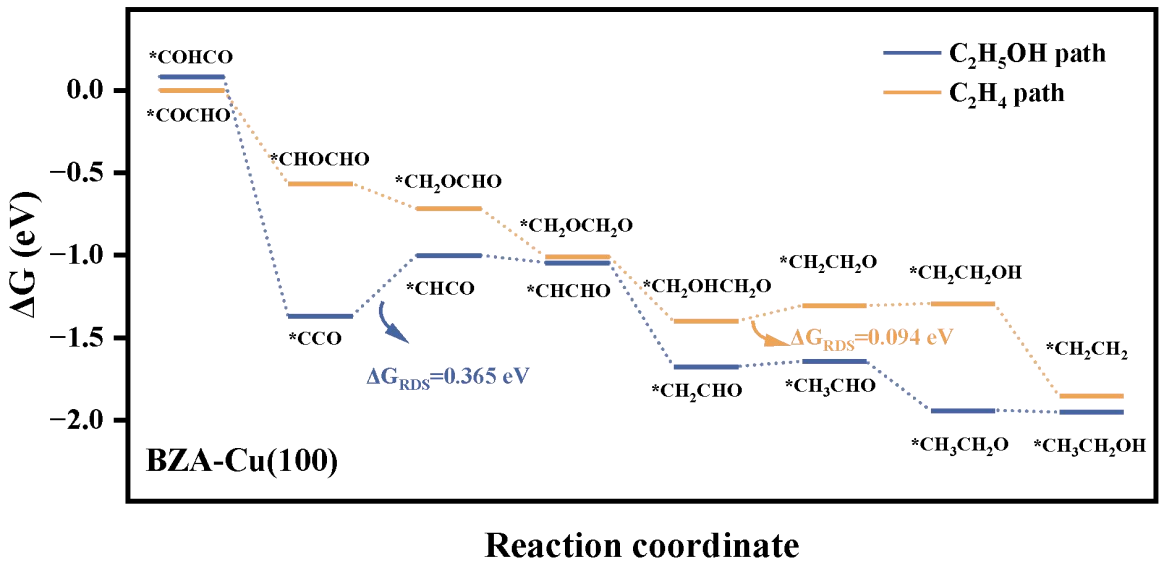

Supplementary Figure 7. Free energy diagrams of the pathways for ethylene and ethanol production on the BZA-Cu(100) surface.

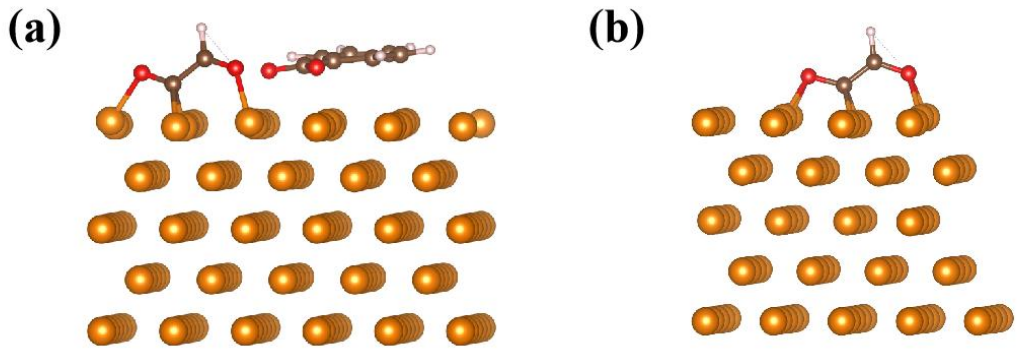

Supplementary Figure 8. Adsorption configurations of CHOCO on (a) BZA-Cu (100) and (b) Cu (100) surface.

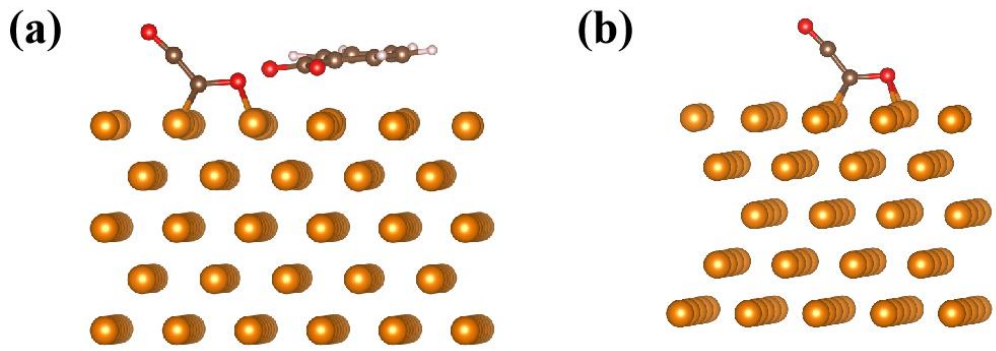

Supplementary Figure 9. Adsorption configurations of COCO on (a) BZA-Cu (100) and (b) Cu (100) surface.

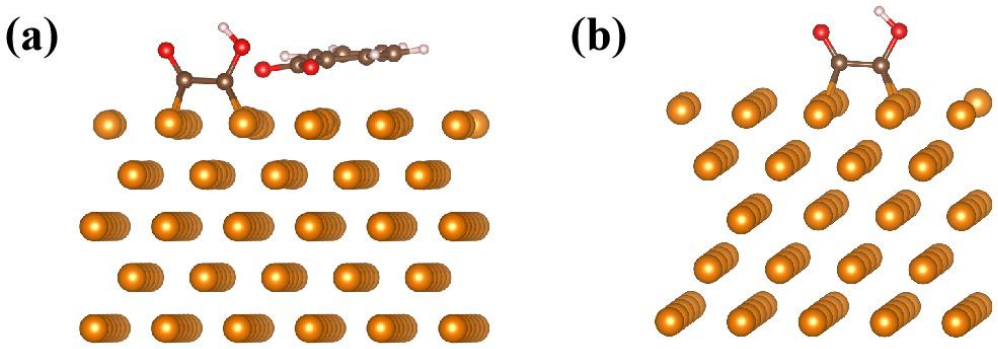

Supplementary Figure 10. Adsorption configurations of COHCO on (a) BZA-Cu (100) and (b) Cu (100) surface.

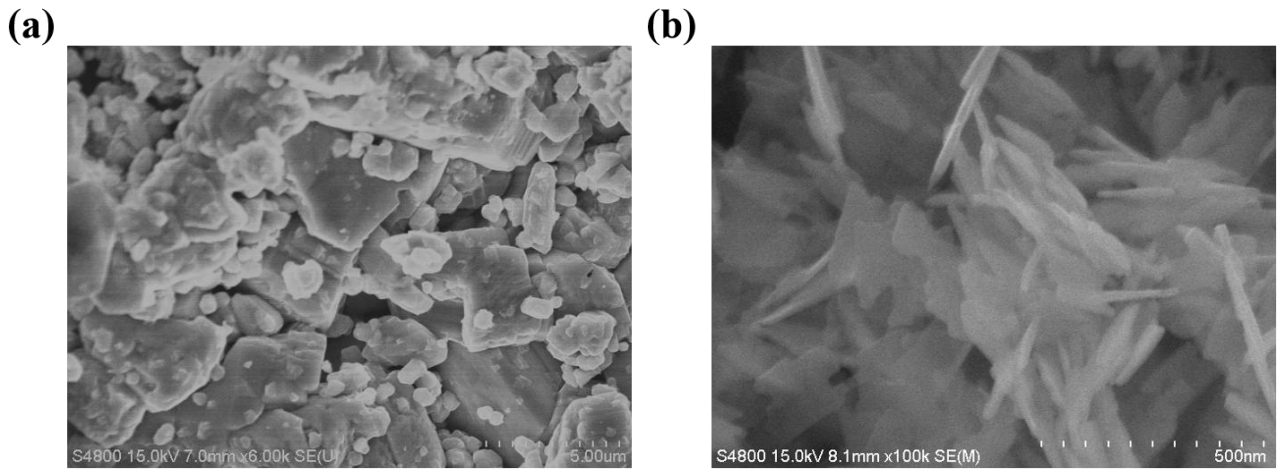

Supplementary Figure 11. SEM images of (a) CuO particles and (b) CuO NS.

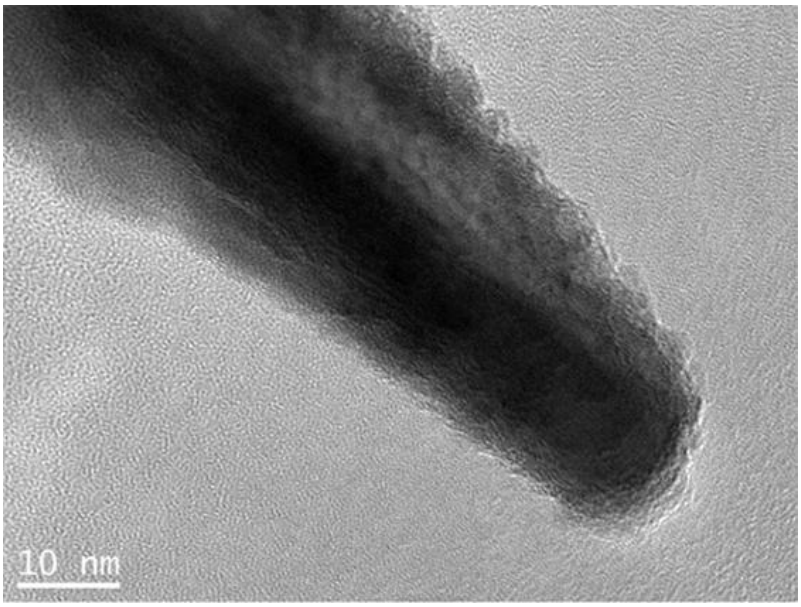

Supplementary Figure 12. HRTEM image of longitudinal cross-sections of CuO NS.

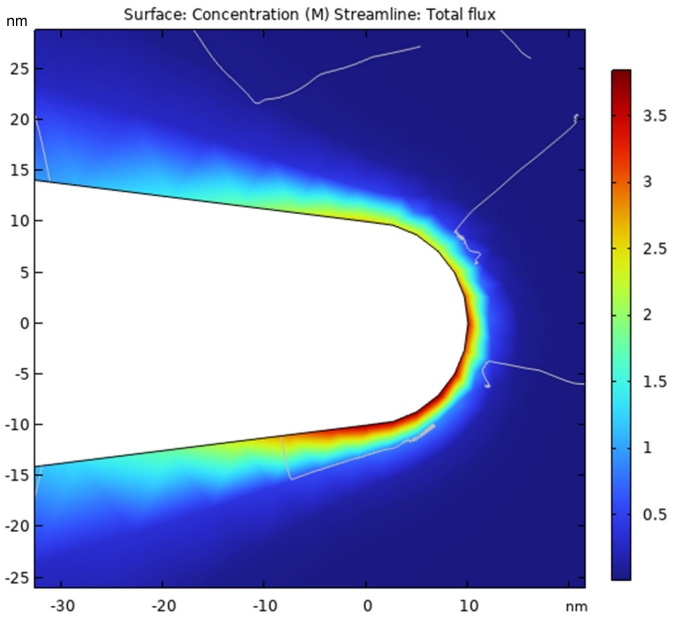

Supplementary Figure 13. The distribution of K^+ concentration at the tip of the CuO NS.

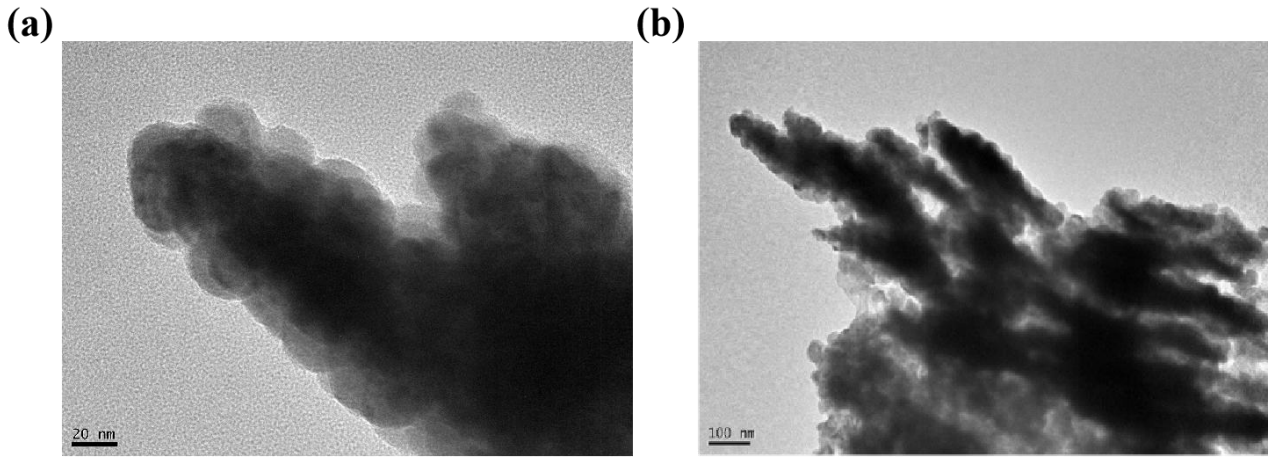

Supplementary Figure 14. HRTEM images of TCo-CuO NS catalysts after CO_2RR.

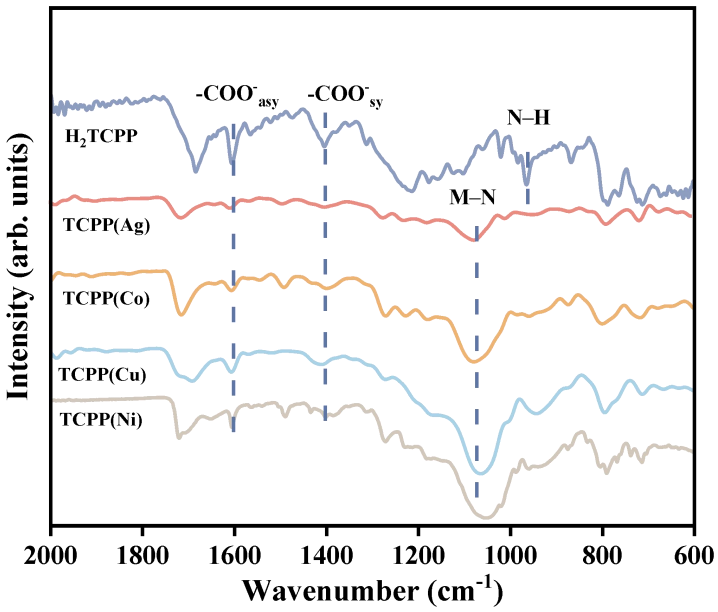

Supplementary Figure 15. ATR-FTIR spectra of H_2TCPP, TCPP(Ag), TCPP(Co), TCPP(Cu), and TCPP(Ni). The positions of the characteristic peaks of each group are indicated in the figure.

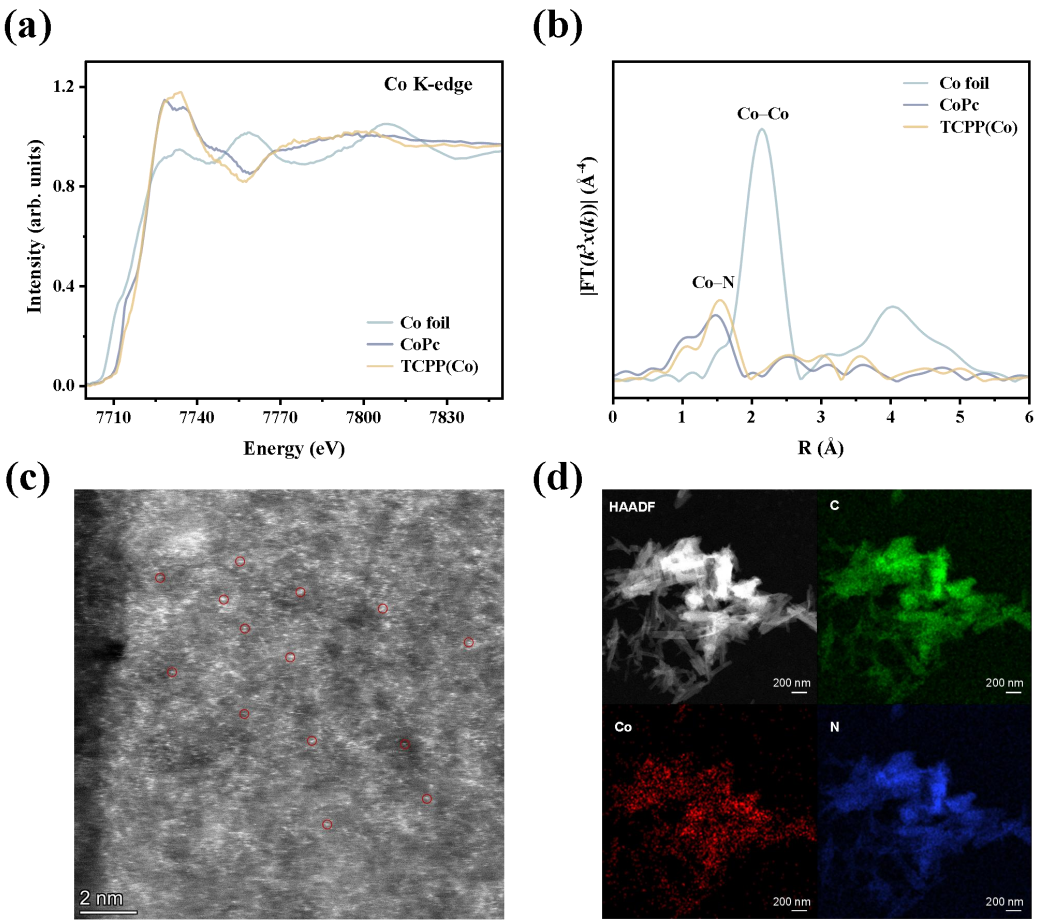

Supplementary Figure 16. (a) Normalized Co K-edge XANES spectra, (b) FT-EXAFS spectra of TCPP(Co), with Co foil and cobalt phthalocyanine (CoPc) as references. (c) AC-STEM image (isolated Co atoms are highlighted by red circles), (d) HAADF-STEM image and the corresponding EDS elemental mapping of TCPP(Co).

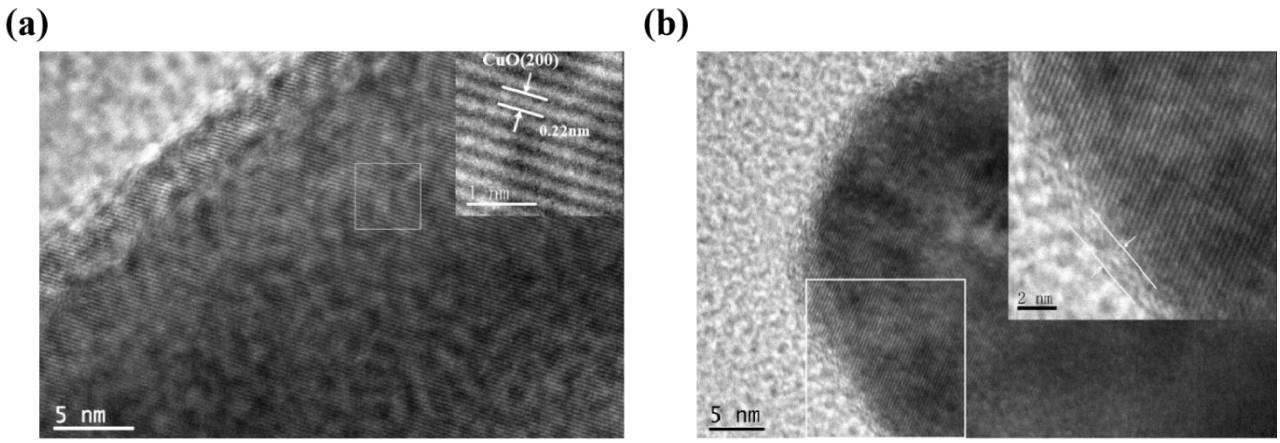

Supplementary Figure 17. HRTEM images of TCo-CuO NS before CO_2RR, (a) the top right corner shows a partial enlargement. (b) Amorphous phase layers have been labelled.

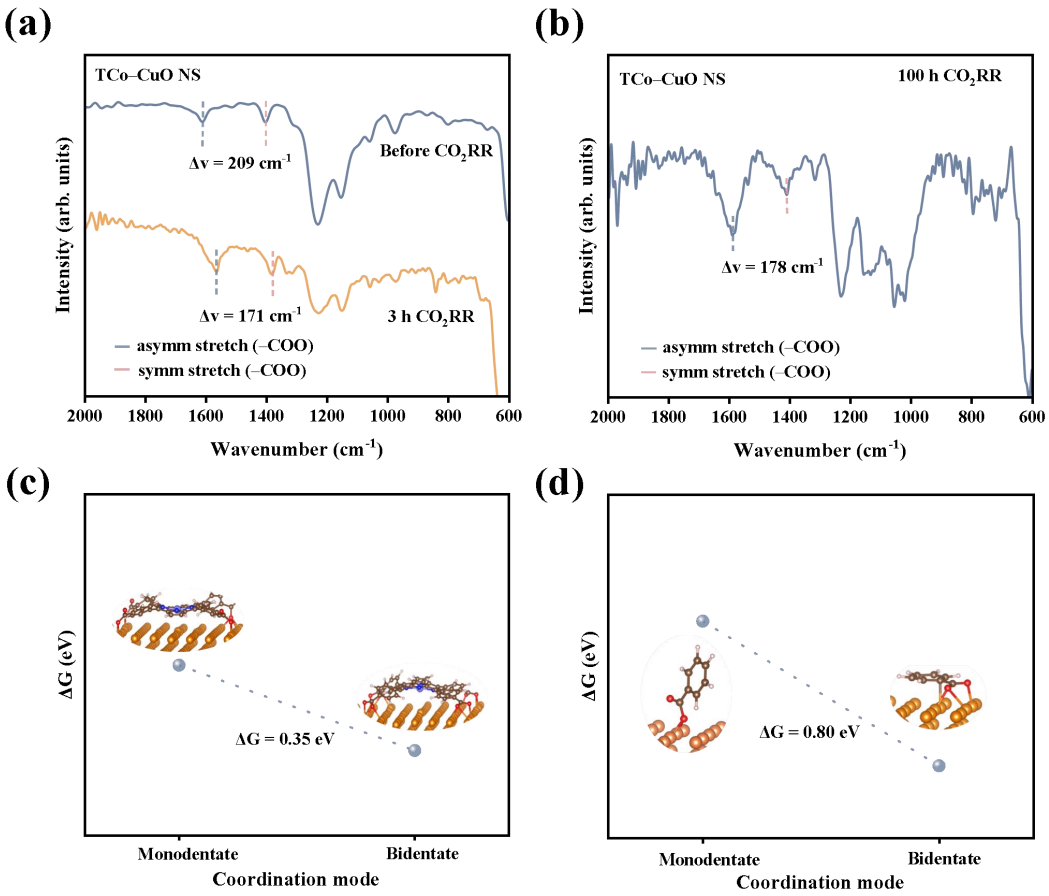

Supplementary Figure 18. ATR-FTIR spectra of TCo-CuO NS (a) before and after 3 h CO_2RR test, (b) after 100 h CO_2RR test at 0.2 A cm^{-2}. Calculated relative free energy (ΔG) profiles comparing the monodentate and bidentate configurations for (c) the complete TCPP(Co) complex and (d) the simplified benzoic acid (BZA) model. The bidentate coordination is thermodynamically preferred in both systems.

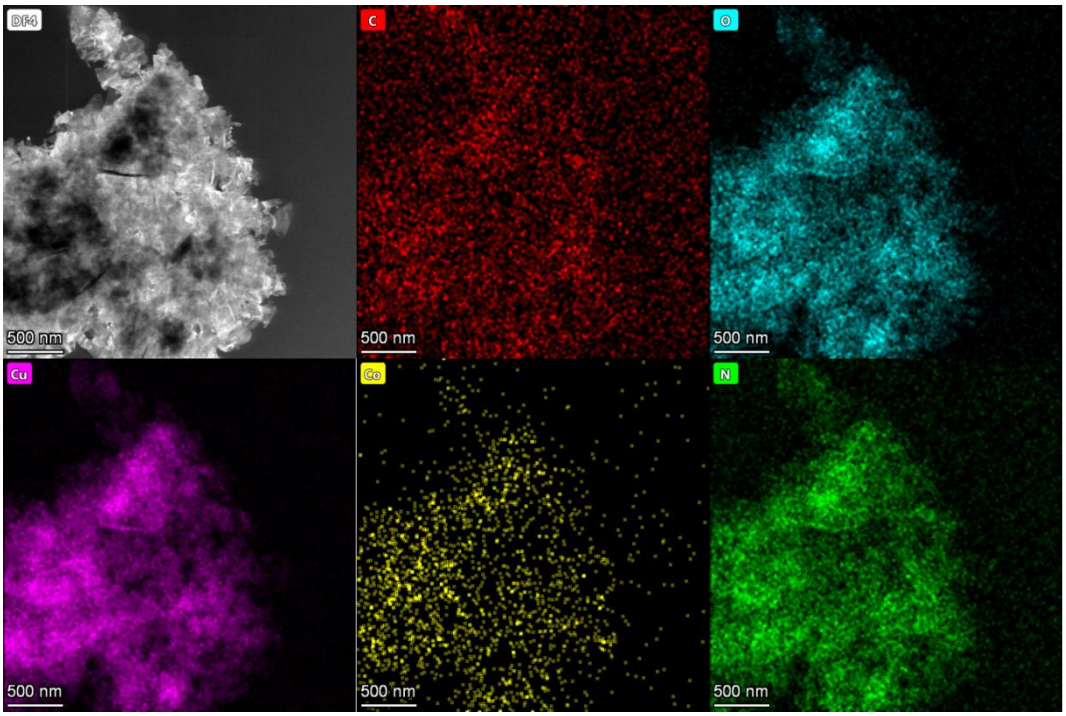

Supplementary Figure 19. HAADF-STEM image and the corresponding EDS elemental mapping of TCo-CuO NS before CO_2RR.

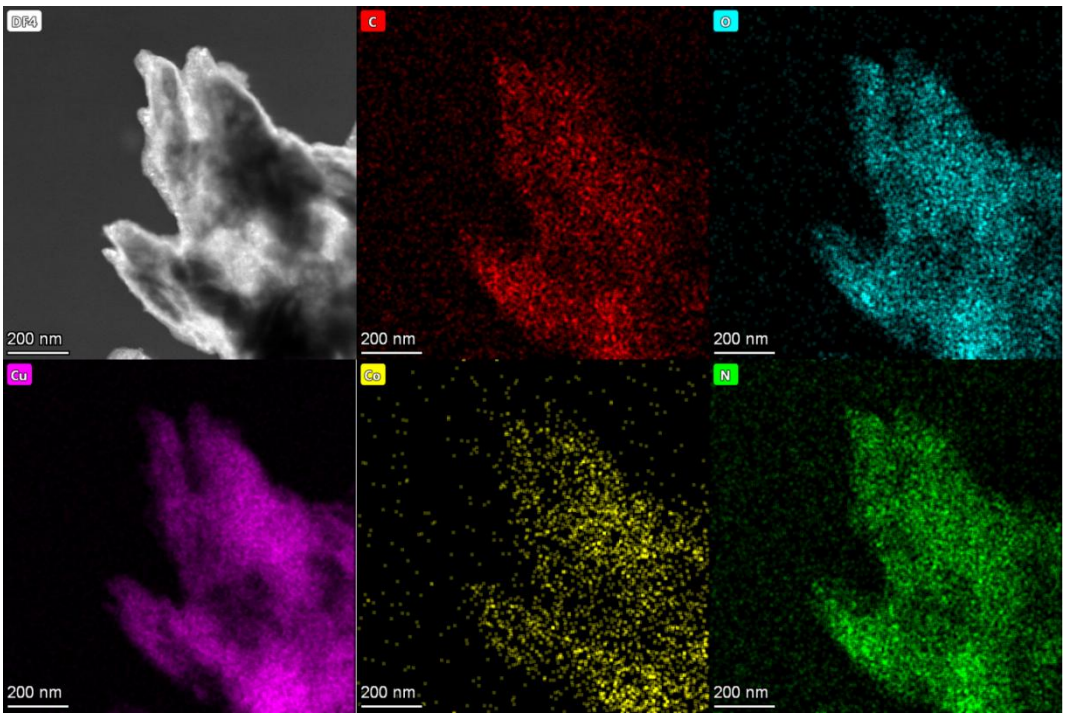

Supplementary Figure 20. HAADF-STEM image and the corresponding EDS elemental mapping of TCo-CuO NS after 3 h CO_2RR.

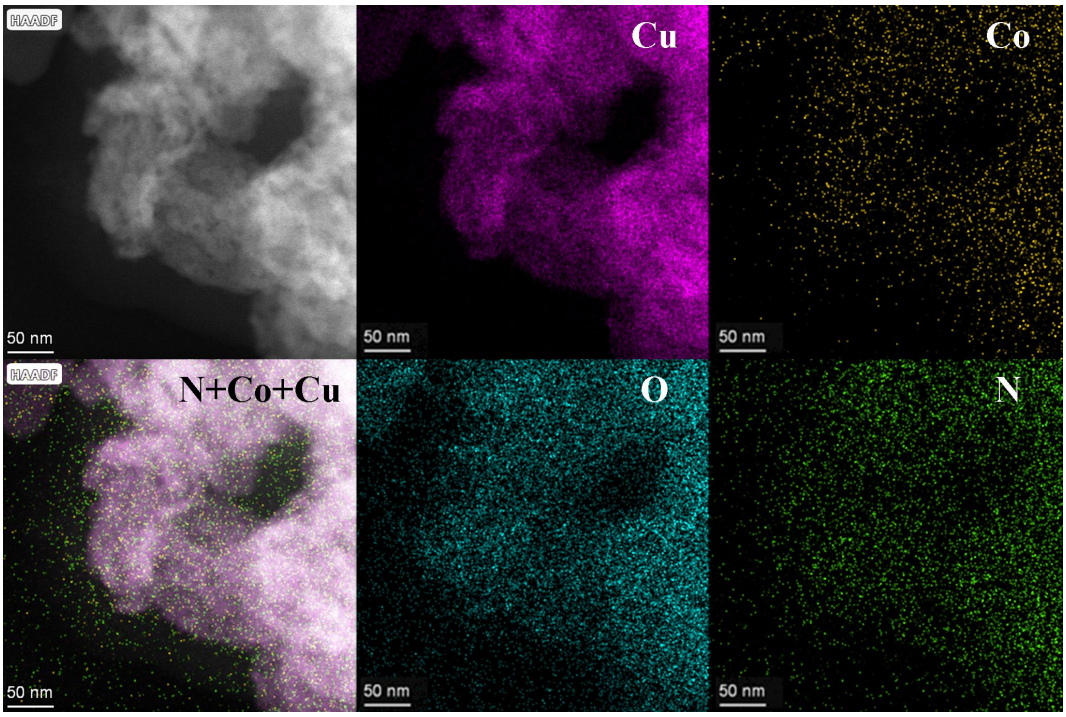

Supplementary Figure 21. HAADF-STEM image and the corresponding EDS elemental mapping of TCo-CuO NS after 100 h CO_2RR at 0.2 A cm^{-2}.

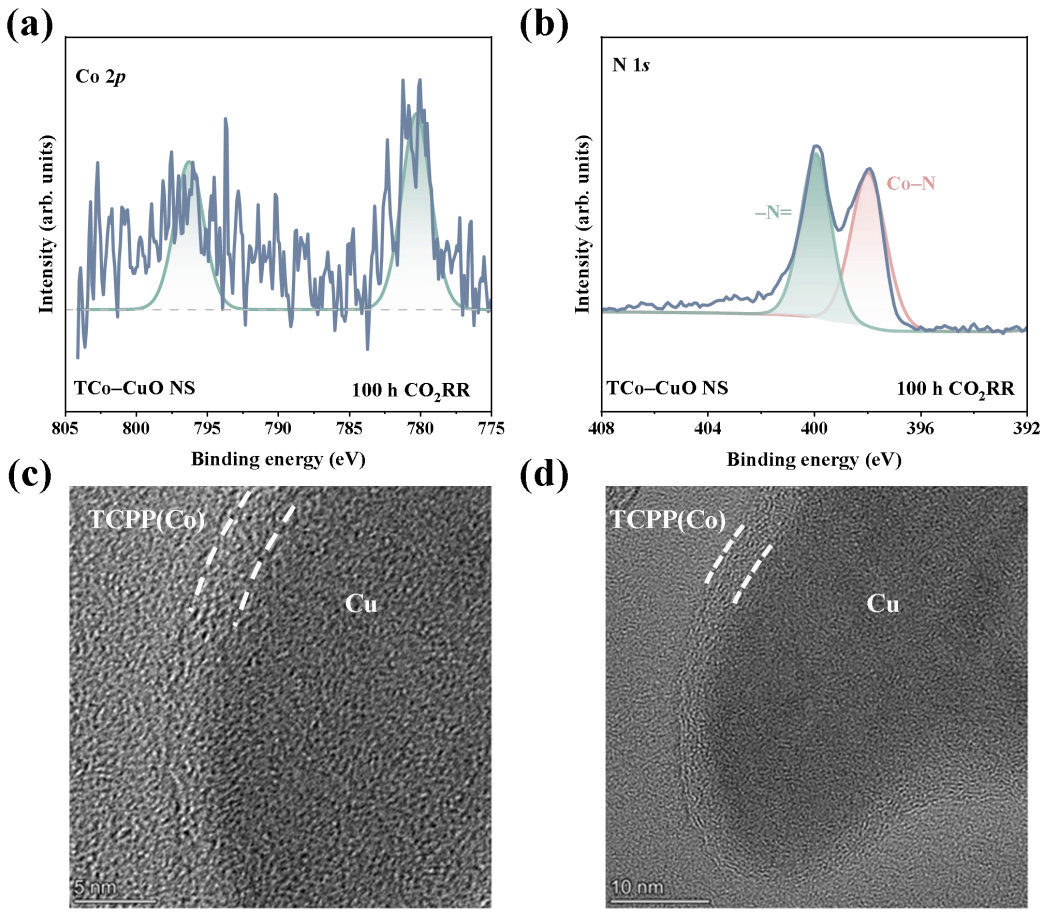

Supplementary Figure 22. High-resolution XPS spectra of TCo-CuO NS (a) Co 2*p* and (b) N 1*s*. (c, d) HRTEM image of TCo-CuO NS, the thin layer of TCPP(Co) was marked by white line, after 100 h stability test at 0.2 A cm^{-2}.

Supplementary Note 2: We acquired the Co 2p and N 1s high-resolution XPS spectra of the post-100 h sample (**Supplementary Figure 22a-22b**). These spectra perfectly match those of the pristine catalyst, with no emergence of zero-valent Co or CoO species, confirming that the Co–N_4 coordination centers remain highly stable under prolonged cathodic polarization.

Supplementary Note 3: To provide even more comprehensive proof, we also supplemented post-100 h HRTEM image, which shows the preserved nanoscale molecular layer (**Supplementary Figure 22c-22d**). Along with an accelerated continuous ICP leaching test to further corroborate the excellent anchoring stability of TCPP(Co).

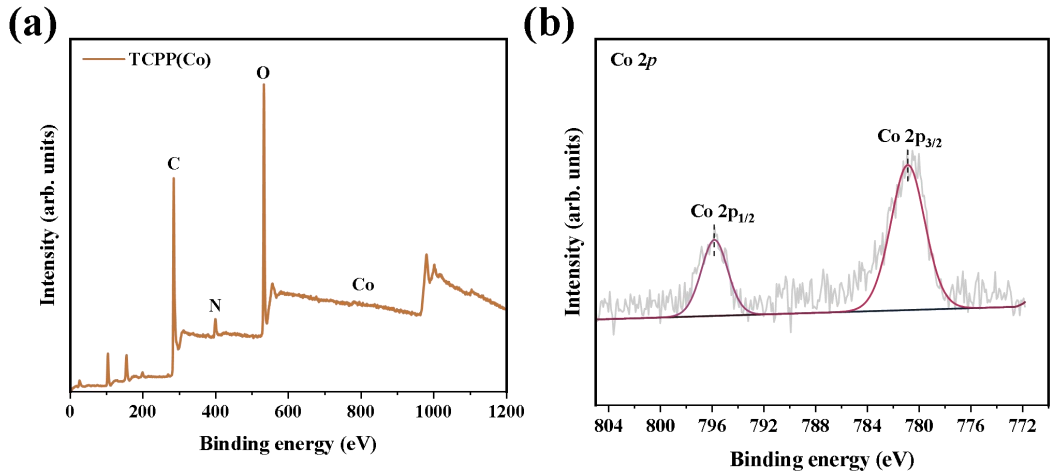

Supplementary Figure 23. XPS spectra of TCPP(Co) (a) survey scan and (b) Co 2*p*.

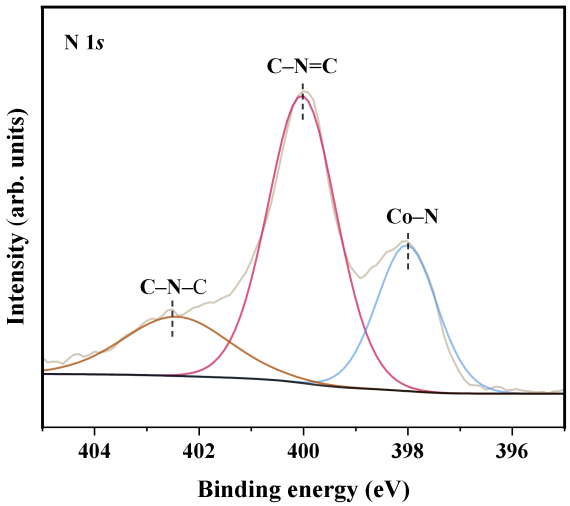

Supplementary Figure 24. N 1*s* XPS analysis of TCPP(Co).

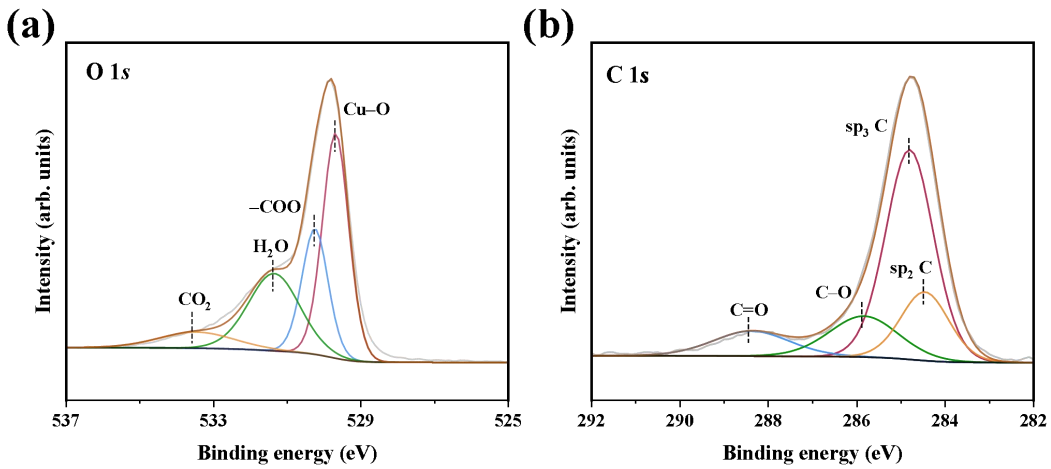

Supplementary Figure 25. XPS analysis of TCo-CuO NS catalysts focusing on (a) O 1*s* and (b) C 1*s*.

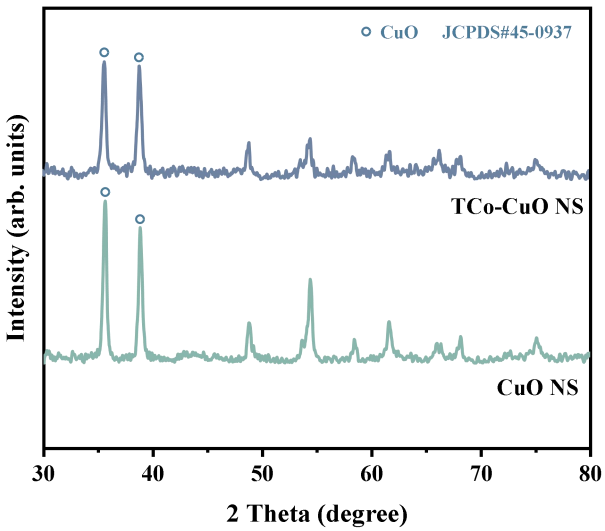

Supplementary Figure 26. XRD patterns of TCo-CuO NS and CuO NS.

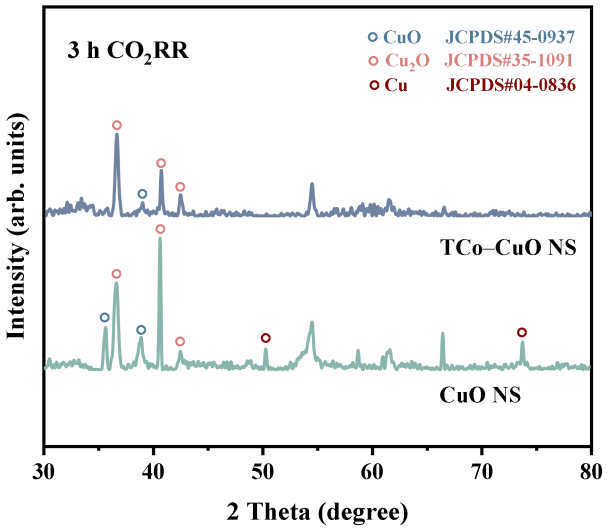

Supplementary Figure 27. XRD patterns of TCo-CuO NS and CuO NS after CO_2RR.

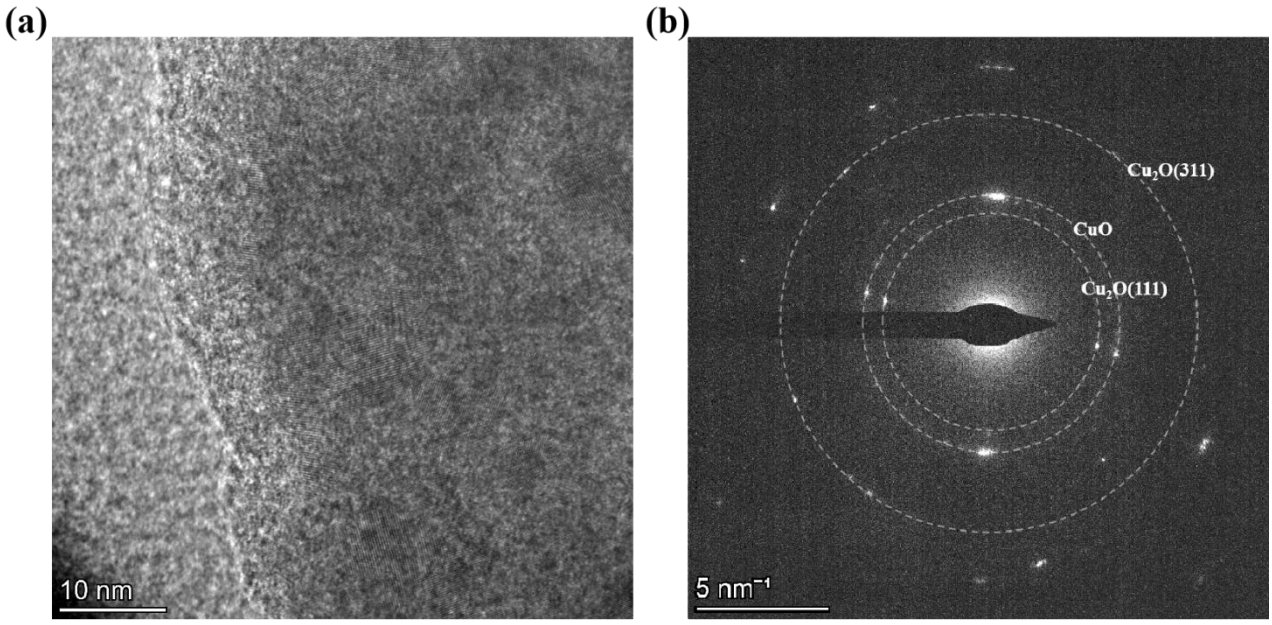

Supplementary Figure 28. (a) HRTEM (b) Selected area electron diffraction image of TCo-CuO NS after 3 h CO_2RR.

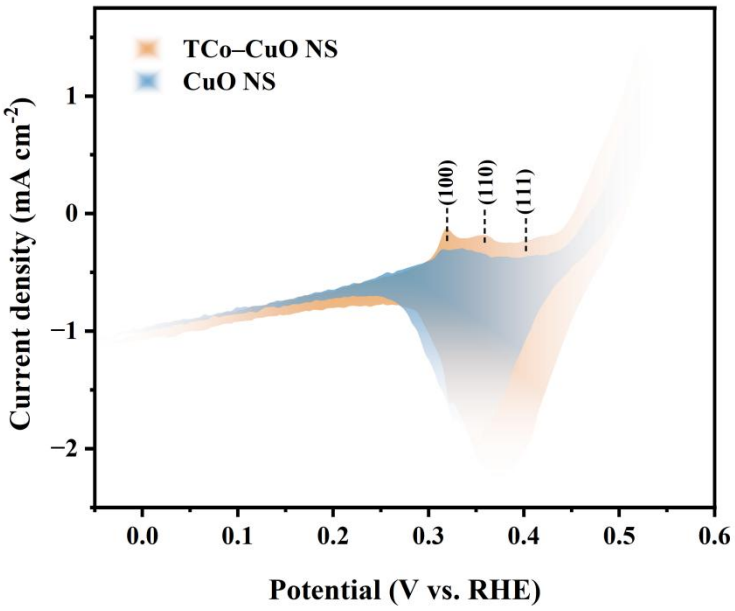

Supplementary Figure 29. CV curves for OH^- adsorption on TCo-CuO NS and CuO NS in Ar-saturated 1 M KOH aqueous solution.

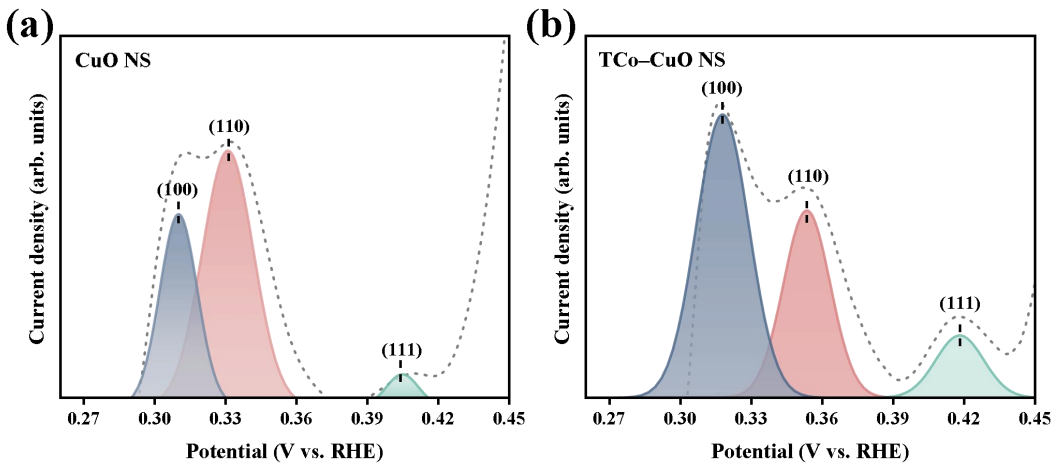

Supplementary Figure 30. Fitted peak splitting results of CV curves for OH^- adsorption on (a) CuO NS and (b) TCo-CuO NS.

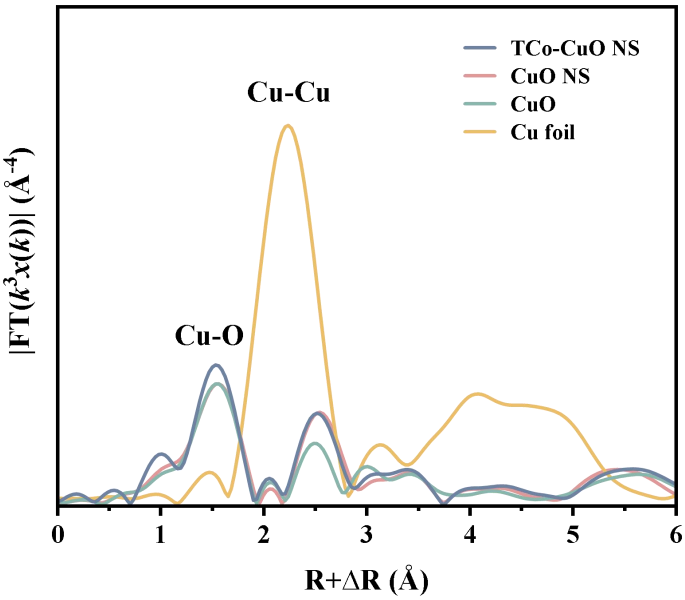

Supplementary Figure 31. Cu K-edge FT-EXAFS spectra, with Cu foil and CuO as references.

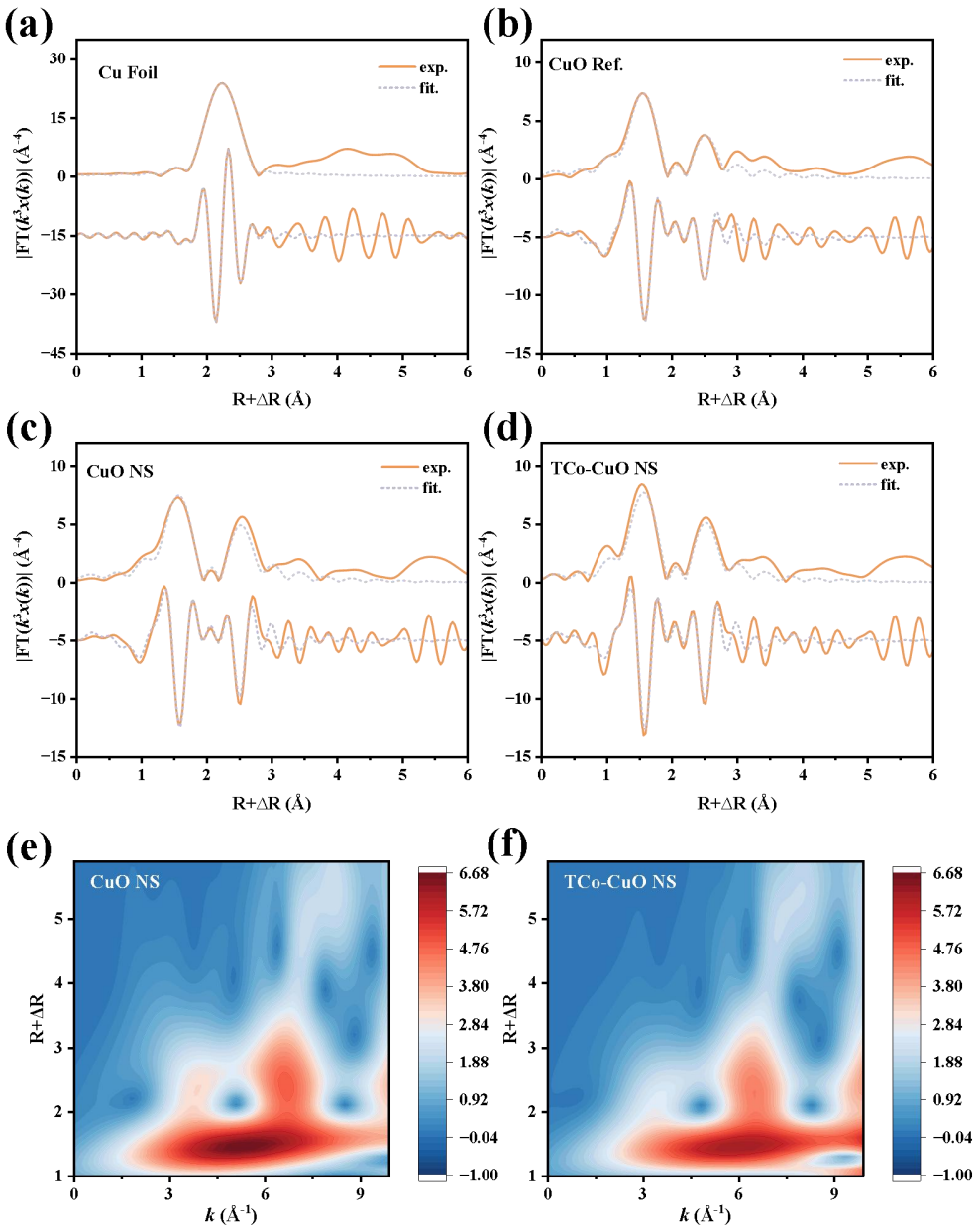

Supplementary Figure 32. K-space and R-space of Cu K-edge EXAFS fitting curves of (a) Cu foil; (b) CuO Ref.; (c) CuO NS (d) TCo-CuO NS with phase correction. Morlet wavelet transform contour plots for the k^3weighted EXAFS of (e) CuO NS (f) TCo-CuO NS.

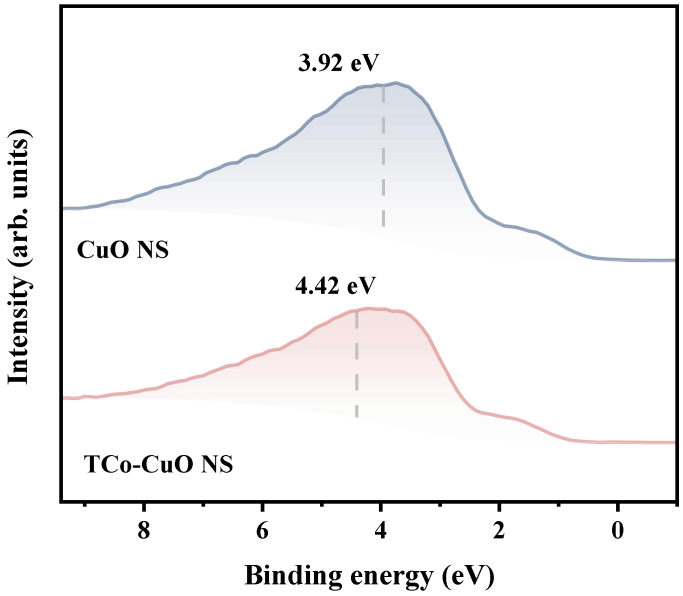

Supplementary Figure 33. Valence band XPS spectra of CuO NS and TCo-CuO NS.

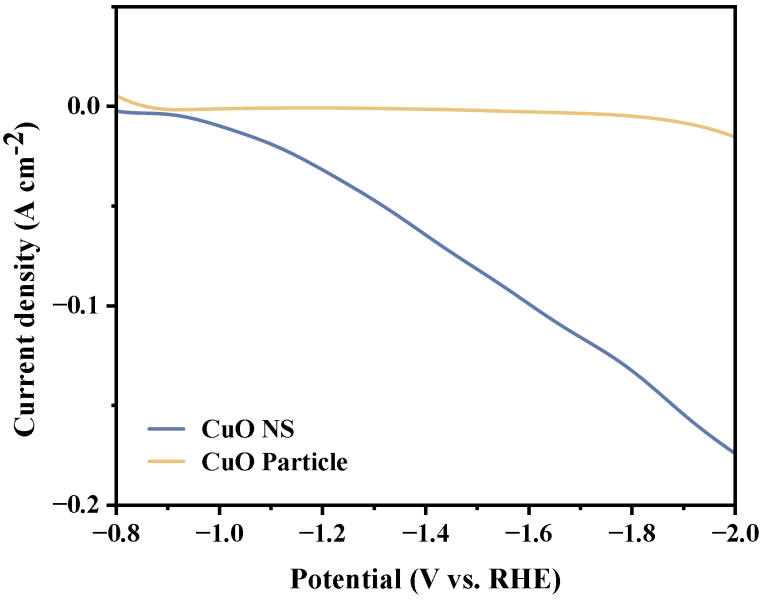

Supplementary Figure 34. LSV curves for CuO NS and CuO particles in the presence of 1 M KCl at pH 2.

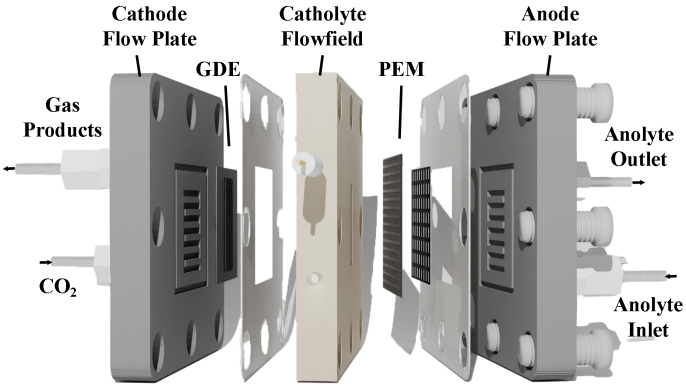

Supplementary Figure 35. Schematic of the three-electrode flow cell.

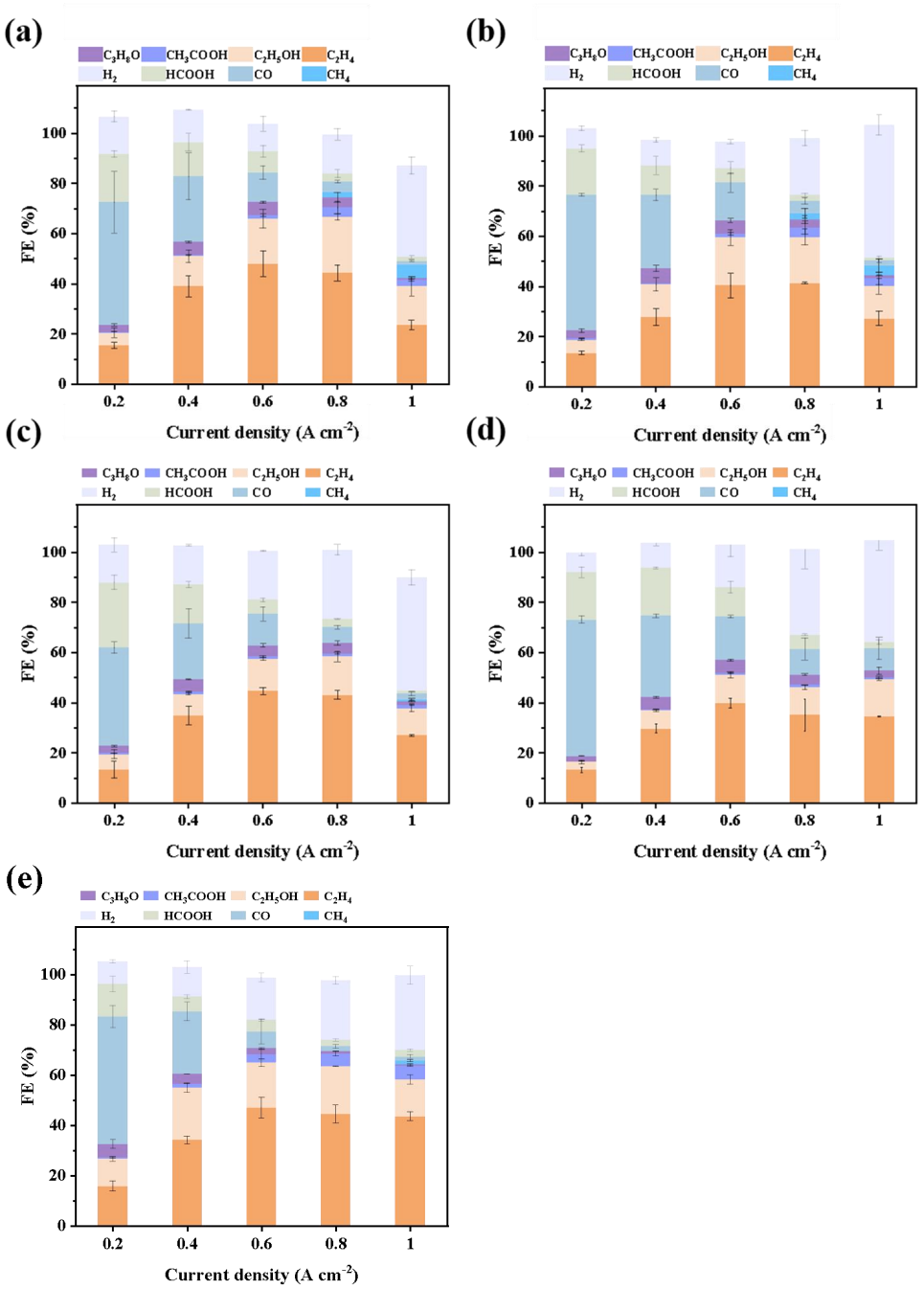

Supplementary Figure 36. The CO_2RR product distributions obtained at different current densities (a) TCu-CuO NS, (b) TAg-CuO NS, (c) TNi-CuO NS, (d) CuO NS, (e) H_2TCPP-CuO NS in the presence of 1 M KCl at pH 2.

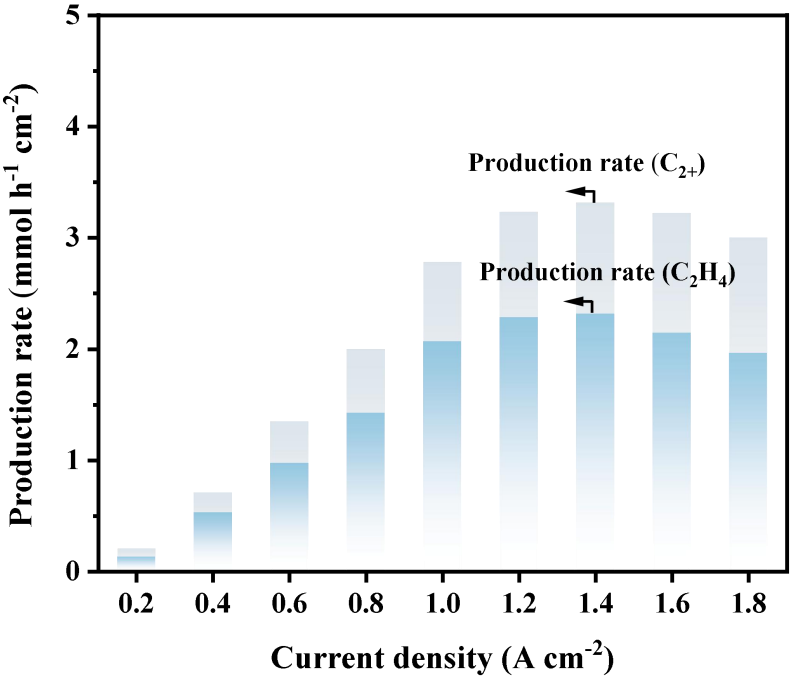

Supplementary Figure 37. Production rate of C_2H_4 and C_{2+} products for TCo-CuO NS calculated based on FEs.

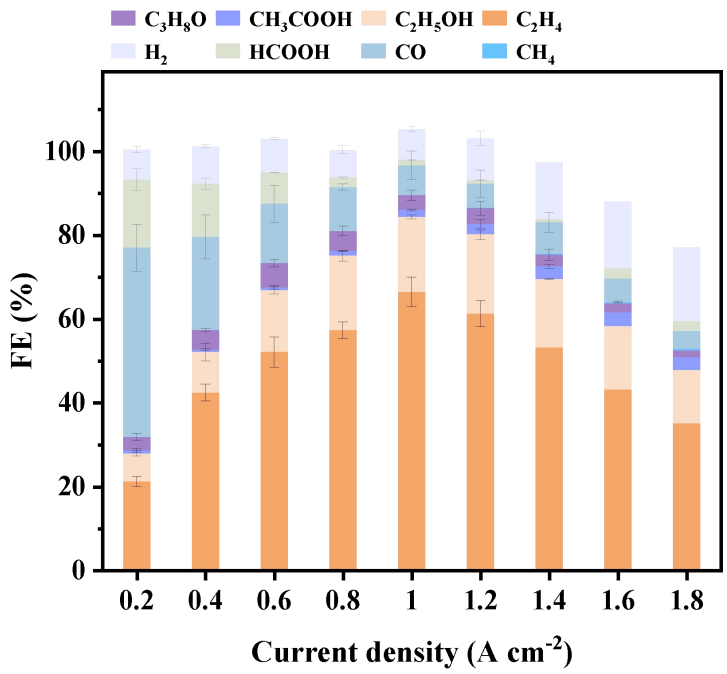

Supplementary Figure 38. The CO_2RR product distributions obtained for TCo-CuO NS in the range of 0.2-1.8 A cm^{-2} in the presence of 1 M KCl at pH 2.

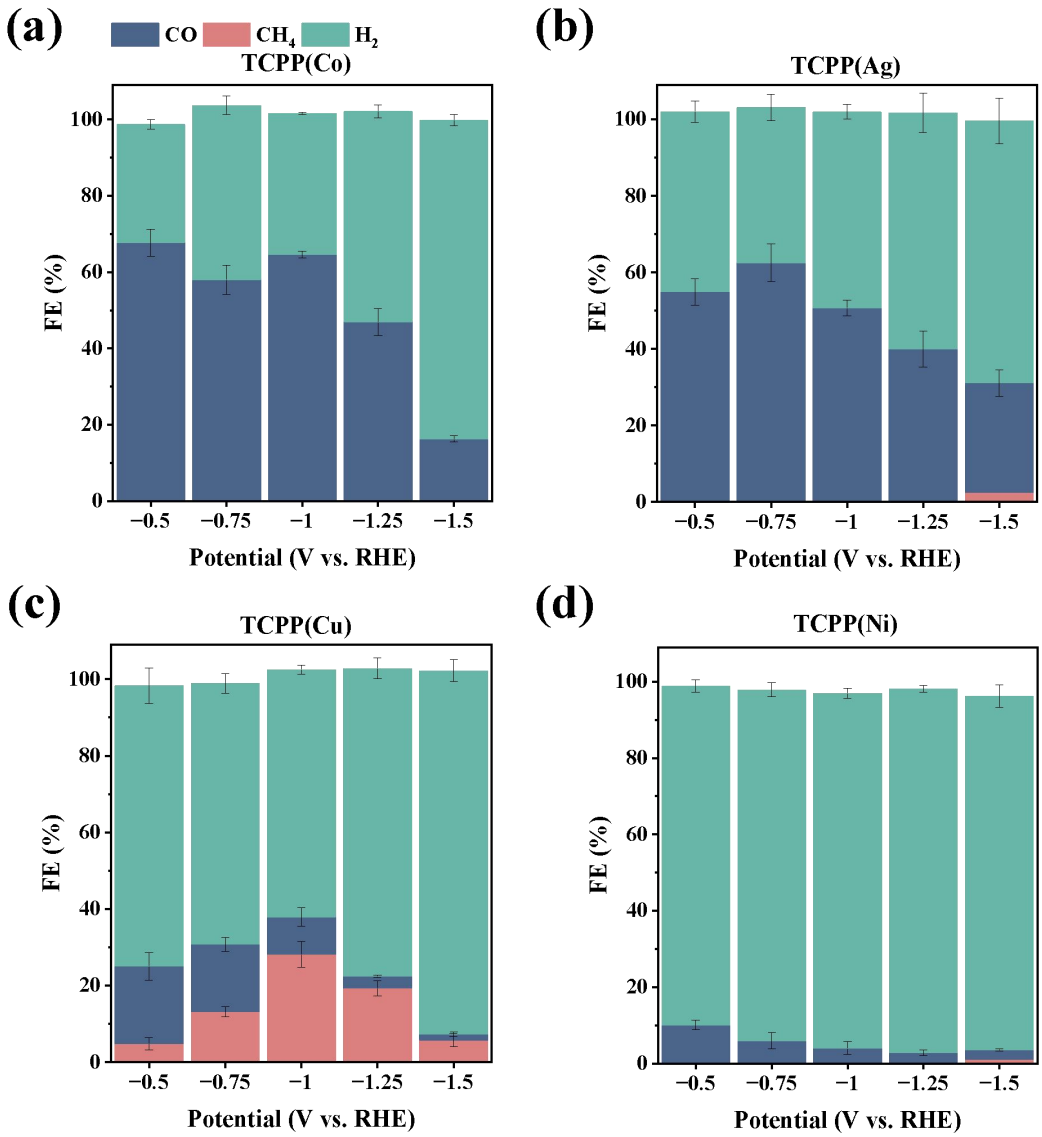

Supplementary Figure 39. FE obtained for (a) TCPP(Co), (b) TCPP(Ag), (c) TCPP(Cu) and (d) TCPP(Ni) (electrolyte: 1 M KOH).

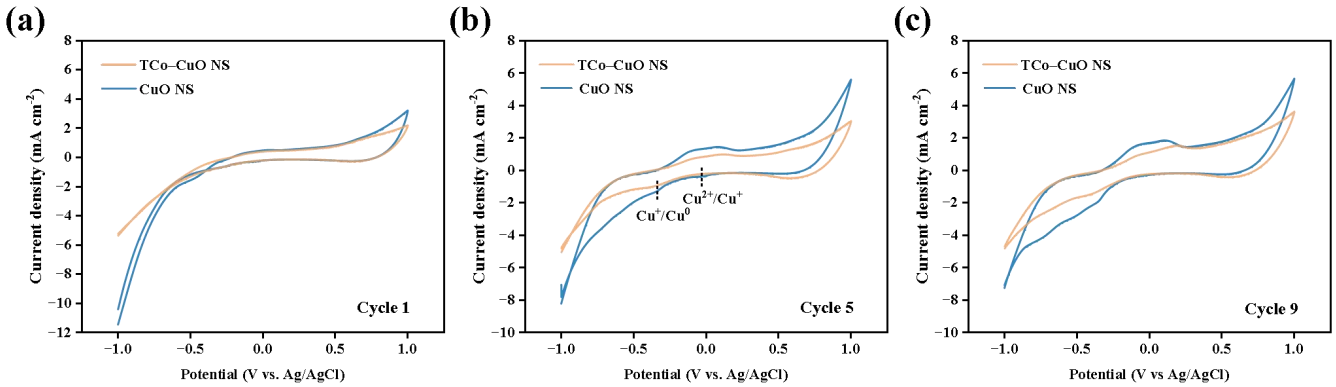

Supplementary Figure 40. CV curves of TCo-CuO NS and CuO NS catalysts at (a) cycle 1, (b) cycle 5, and (c) cycle 9.

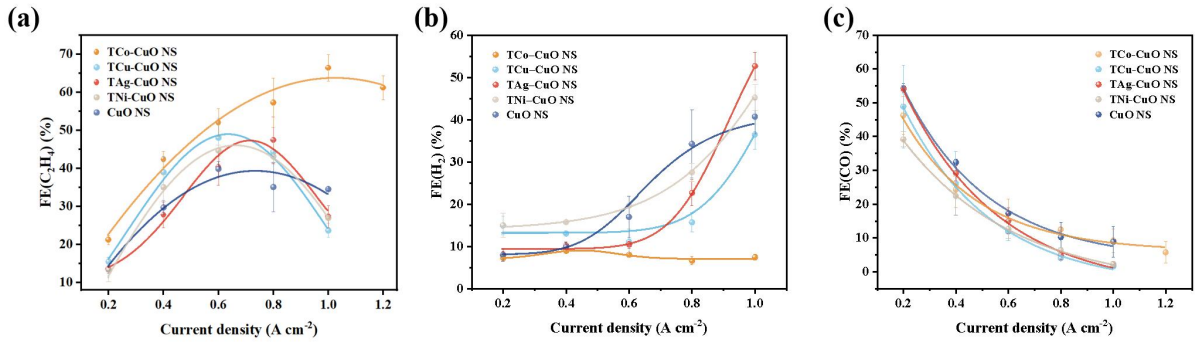

Supplementary Figure 41. (a) C_2H_4, (b) H_2, and (c) CO FE comparison curves for different catalysts in pH 2, 1 M KCl electrolyte.

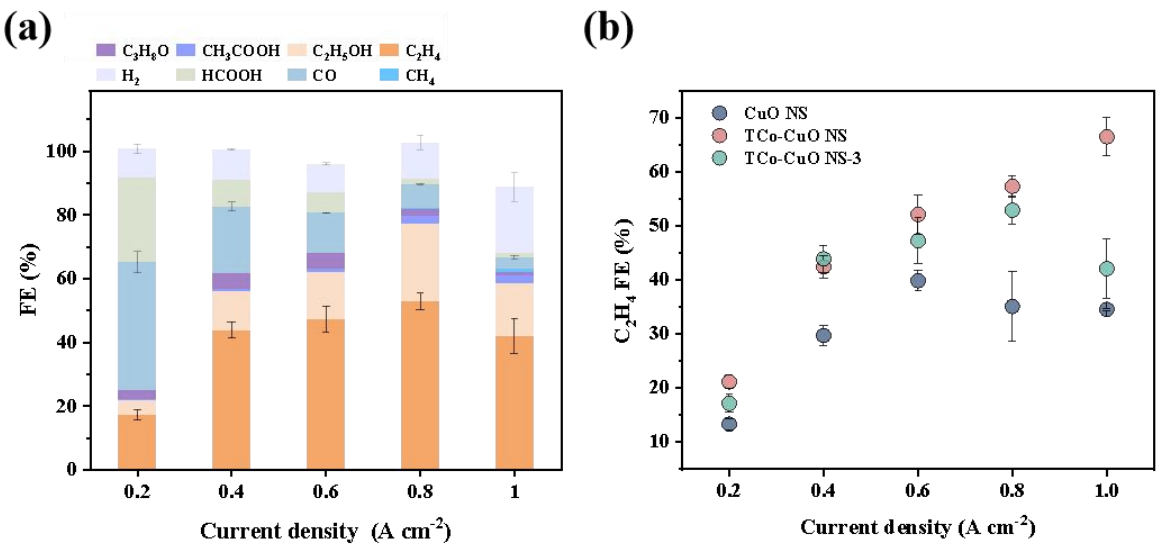

Supplementary Figure 42. (a) The CO_2RR product distributions obtained at different current densities for TCoCS-3. (b) Comparison of C_2H_4 selectivity of catalysts modified with different TCPP(Co) concentrations in pH 2, 1 M KCl electrolyte.

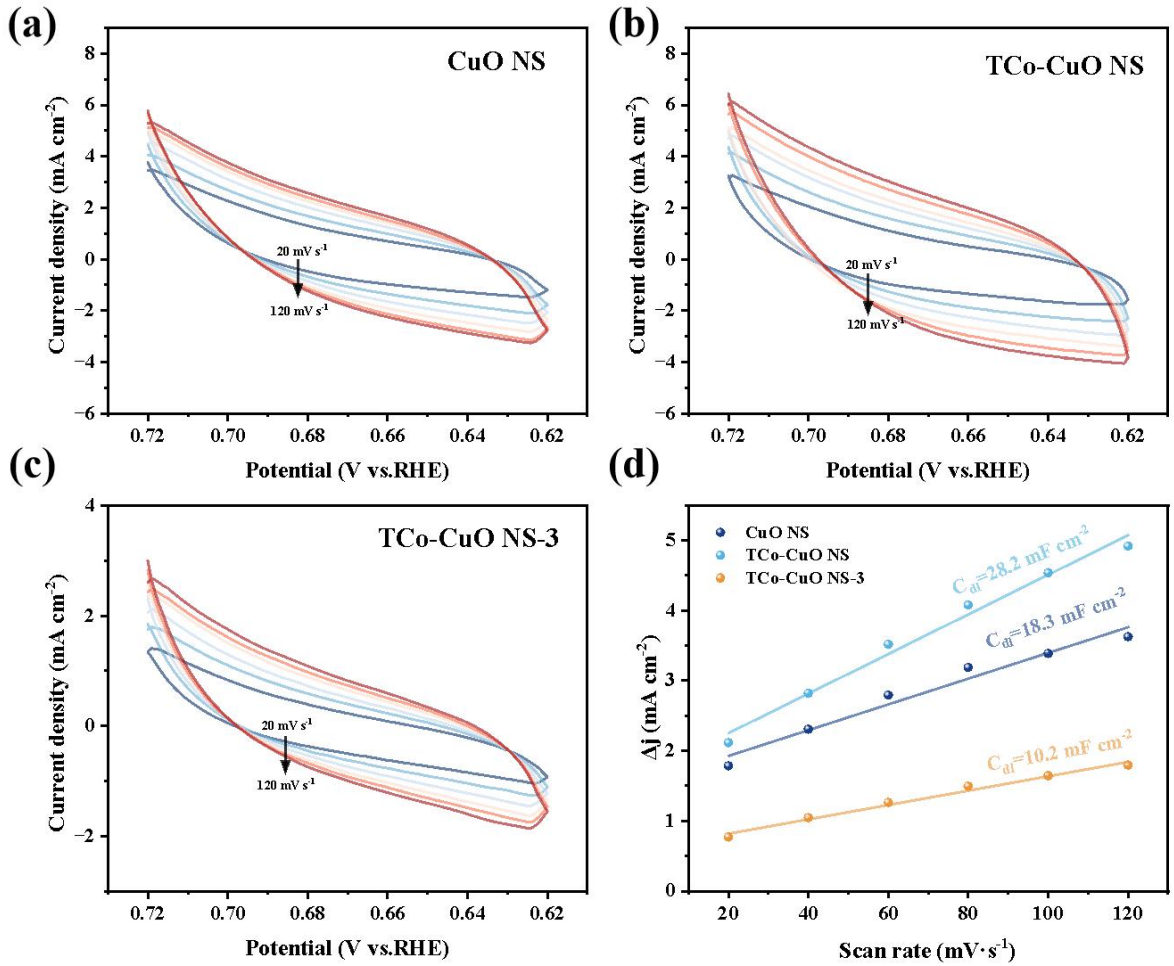

Supplementary Figure 43. CV curves for (a) CuO NS, (b) TCo-CuO NS, and (c) TCo-CuO NS-3 catalyst electrodes recorded in the double layer region at different scan rates. (d) Corresponding charging current densities vs. applied scan rate.

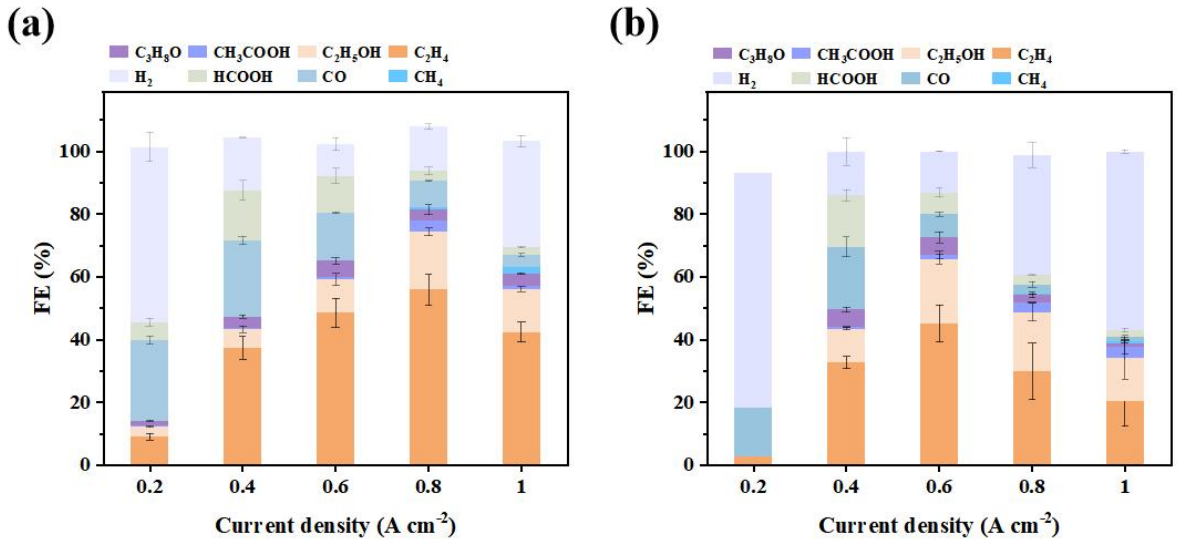

Supplementary Figure 44. The CO_2RR product distributions obtained at different current densities for (a) TCo-CuO NS and (b) CuO NS in pH 0.7, 1 M KCl electrolyte.

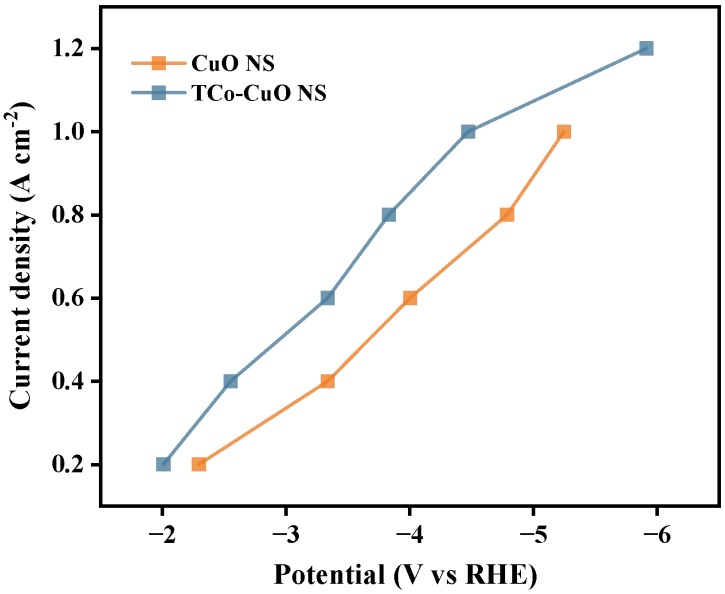

Supplementary Figure 45. Current densities versus applied potential for TCo-CuO NS and CuO NS catalyst.

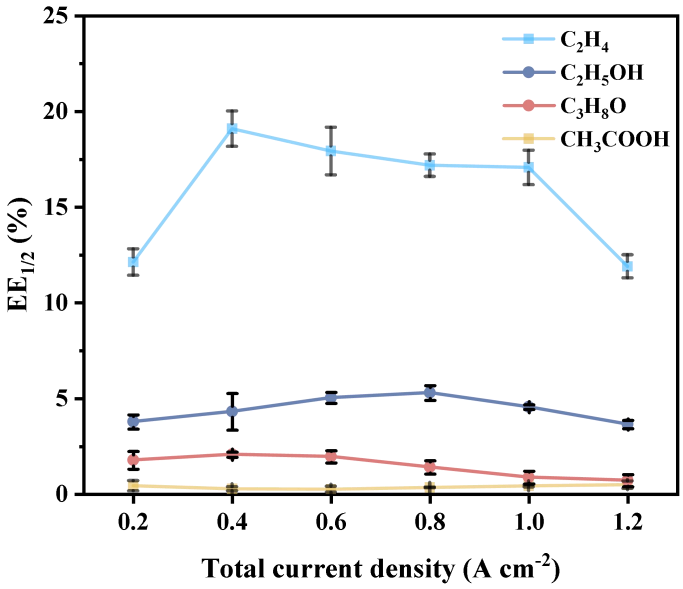

Supplementary Figure 46. The $EE_{1/2}$ of C_{2+} products for TCo-CuO NS in different current density.

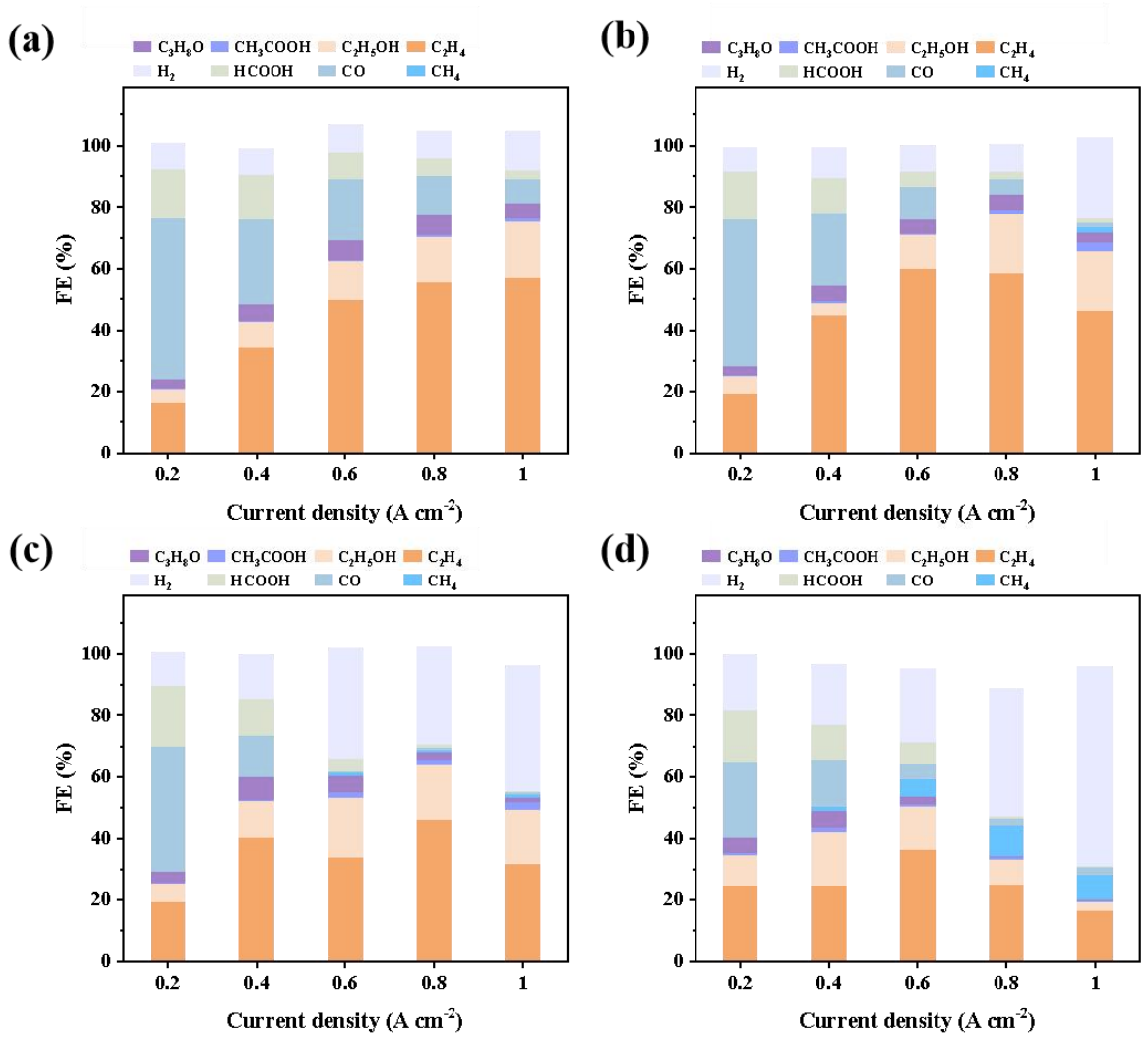

Supplementary Figure 47. The CO_2RR product distributions obtained at different current densities for TCo-CuO NS at a CO_2 flow rate of (a) 25 sccm, (b) 10 sccm, (c) 5 sccm, and (d) 2 sccm.

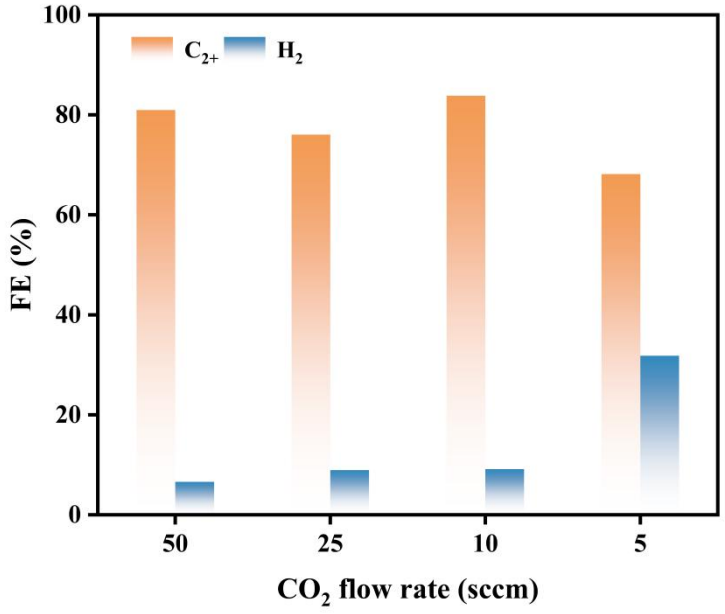

Supplementary Figure 48. FE of C_{2+} products and H_2 obtained for TCo-CuO NS at 0.8 A cm^{-2} using different CO_2 gas flow rates.

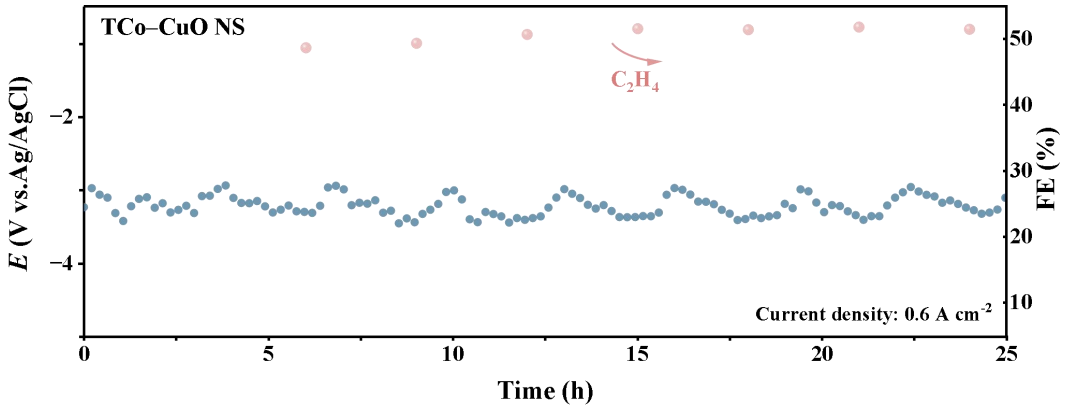

Supplementary Figure 49. Long-term CO_2RR stability of TCo-CuO NS at 0.6 A cm^{-2}.

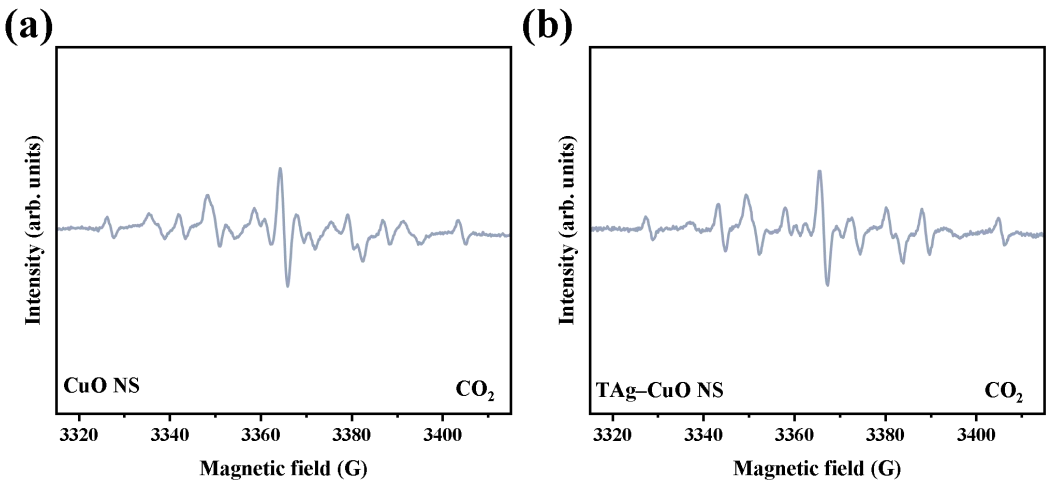

Supplementary Figure 50. In situ EPR spectra recorded in pH 2, 1 M KCl electrolyte under CO_2 atmosphere using DMPO as a trapping reagent, after 10 min of CO_2RR on (a), CuO NS and (b), TAg-CuO NS.

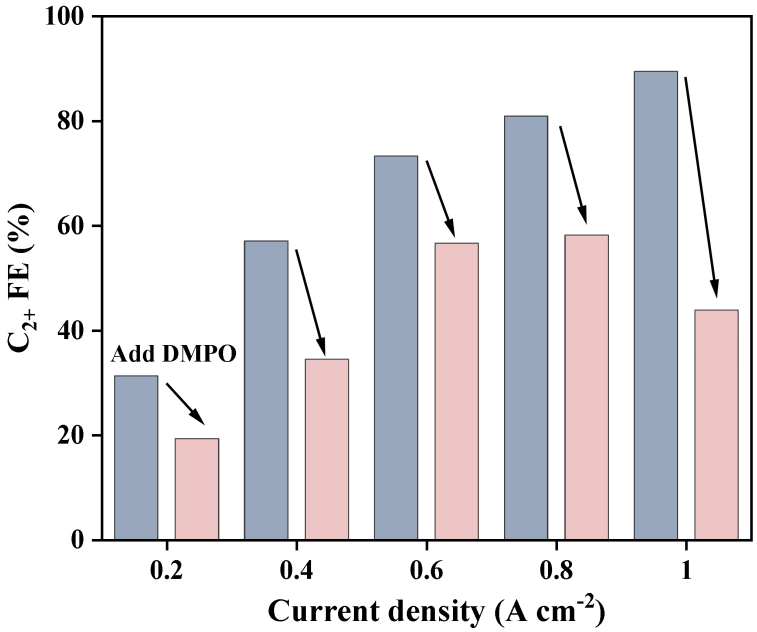

Supplementary Figure 51. Comparison of C_{2+} FE over the TCo-CuO NS catalyst with and without the addition of DMPO.

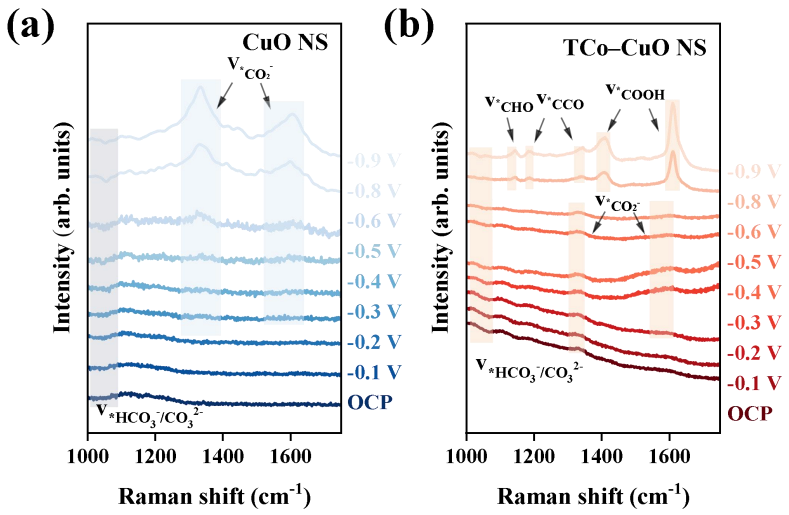

Supplementary Figure 52. In situ SERS spectra of the (a) CuO NS and (b) TCo-CuO NS catalyst in the range 1800-2150 cm^{-1} at various applied potentials.

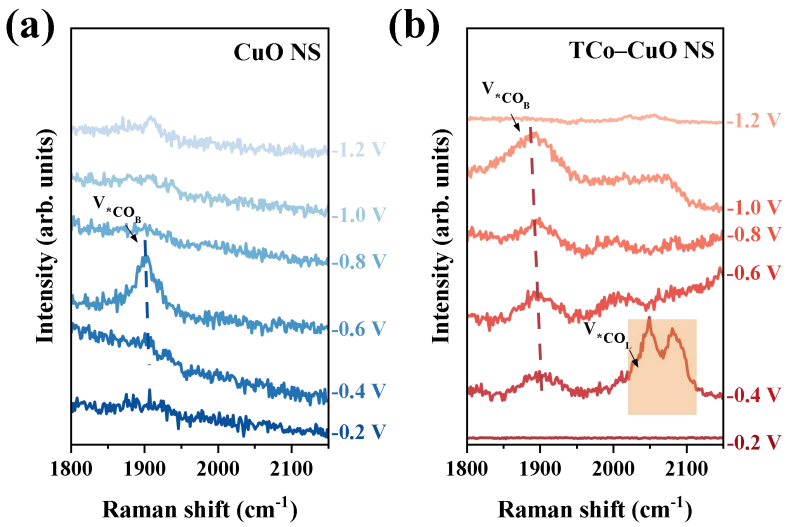

Supplementary Figure 53. In situ SERS spectra of the (a) CuO NS and (b) TCo-CuO NS catalyst in the range 1000-1750 cm^{-1} at OCP to -0.9 V vs. RHE.

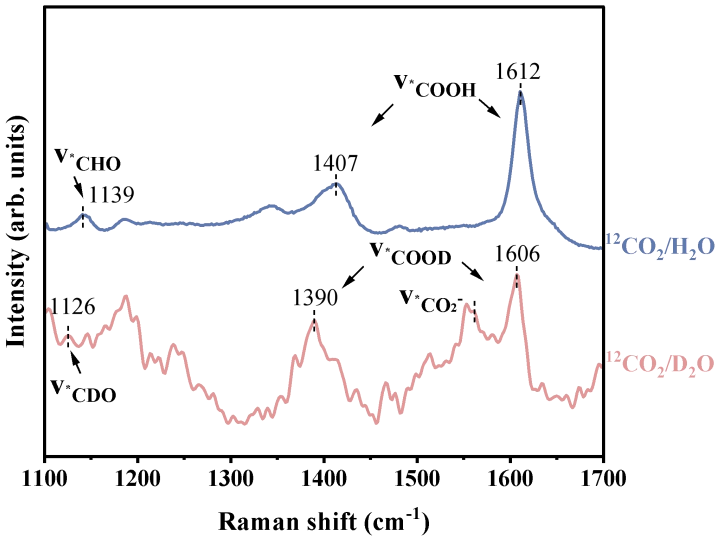

Supplementary Figure 54. Comparison of in situ SERS spectra recorded on TCo-CuO NS during CO_2RR with 0.5 M K_2SO_4/0.005 M H_2SO_4 in H_2O/D_2O at −1.0 V vs. RHE.

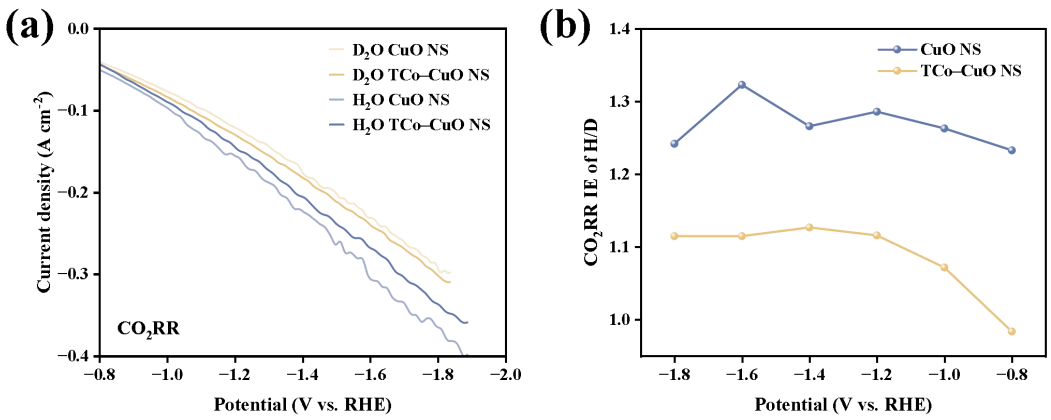

Supplementary Figure 55. (a) LSV curves for CuO NS and TCo-CuO NS with 1 M KCl in H_2O and D_2O. (b) KIE of H/D for CO_2RR with 1 M KCl in H_2O and D_2O.

Supplementary Tables

Supplementary Table 1. Detailed parameters of FEM simulation.

Parameter	Value
a_Cl	8E-10 m
a_H	5.6E-10 m
a_K	6.62E-10 m
a_OH	6E-10 m
D_Cl	1.97E-9 m^2 /s
D_H	9.311E-9 m^2 /s
D_K	2.135E-9 m^2 /s
D_OH	5.273E-9 m^2 /s
z_Cl	-1
z_H	1
z_K	1
z_OH	-1
T0	298.15 K
vis	1E-6 m^2/s
xS	4E-10 m
epsilon_r	80.1

Supplementary Table 2. Theoretical and actual bulk Co/Cu atomic ratios of the optimal (1×) and excessively loaded (3×) TCo–CuO NS catalysts determined by ICP-OES.

Samples	Theoretical Co/Cu atomic ratio	Co/Cu atomic ratio
TCo–CuO NS	0.94%	0.50%
TCo–CuO NS-3	2.82%	0.64%

Supplementary Table 3. Detailed fitting position of TCo–CuO NS and TCo–CuO NS (Post CO_2RR) based on high-resolution XPS spectra.

Catalysts	Cu 2p Fitting position (eV)	Co 2p Fitting position (eV)	Atomic ratio Cu:Co
TCo–CuO NS	934.70/954.51	780.42/795.35	96.63:3.37
TCo–CuO NS (Post CO_2RR)	934.45/954.38	780.47/795.42	97.25:2.75
TCo–CuO NS-3	934.58/954.35	779.75/794.72	96.01:3.99

Supplementary Table 4. Quantitative fitting results of OH^- adsorption experiments.

Electrodes	Crystal plane	Peak area	Percentage (%)	Centre (V)	FWHM
	100	7.66E-6	**55.87**	0.32	0.026
TCo – CuO NS	110	4.53E-6	**32.93**	0.35	0.023
	111	1.54E-6	**11.20**	0.42	0.024
	100	2.37E-06	**33.75**	0.31	0.019
CuO NS	110	4.32E-06	**61.55**	0.33	0.026
	111	3.29E-07	**4.70**	0.40	0.016

Supplementary Table 5. Fitting parameters of Cu K-edge EXAFS spectra[a].

Samples	Shell	CN	R (Å)	Δ E_0 (eV)	R-factor (%)
Cu Foil	Cu – Cu	12	2.56	4.37±0.70	0.46
CuO Ref.	Cu – O1	4	1.95	9.34±1.11	1.23
	Cu – O2	2	2.77		
CuO NS	Cu – O1	3.88±0.45	1.95	10.31±0.80	2.55
	Cu – O2	2.85±0.74	2.77		
TCo – CuO NS	Cu – O1	3.89±0.34	1.95	10.20±0.60	2.59
	Cu – O2	2.89±0.56	2.77		

[a] CN: coordination number; R: distance between absorber and backscatter atoms; Δ E_0: inner potential correction. R factor: goodness of the fitting. S_0^2 of CuO NS, TCo–CuO NS was set to 0.752 according to the experimental FT-EXAFS fit of CuO Ref. reference by fixing CN as the known crystallographic value (4/2). Fitting range: k (Å): 3-11, R (Å): 1-2.8.

Supplementary Table 6. Capacitance values and surface roughness coefficients of electrodes measured using CV method.

Electrodes	**Capacitance (mF cm^{-2})**	**Surface roughness factor**
CuO NS	18.3	1
TCo-CuO NS	28.2	1.54
TCo-CuO NS-3	10.2	0.56

Supplementary Table 7. Performance and conditions of CO_2RR catalysts compared with other recent reports.

Reference	electrolyte	Cell configuration	C_{2+} FE (%)	C_{2+} current density (A cm^{-2})	Durability	C_2H_4 R_i (mmol h^{-1} cm^{-2})
This work	**pH 2, 1 M KCl**	**flow cell**	**89.5**	**1.04**	**100 h**	**2.28**
Ref.[1]	1 M KCl and 0.05 M H_2SO_4	flow cell	89.0	0.45	12 h	0.705
Ref.[2]	pH 1.8, 0.5 M K_2SO_4	flow cell	82.2	1.137	8 h	/
Ref.[3]	0.5 M H_3PO_4, 0.5 M KH_2PO_4 and 2.5 M KCl	flow cell	82.0	0.66	16 h	1.37
Ref.[4]	pH 1, 3 M KCl	flow cell	75.0	0.15	30 h	0.497
Ref.[5]	pH 2, 0.5 M K_2SO_4	flow cell	42.2	0.14	9h	0.27
Ref.[6]	1 M H_3PO_4 3 M KCl	flow cell	48.0	0.58	10 h	/
Ref.[7]	0.2 M H_2SO_4	flow cell	80.0	0.08	155 h	0.25
Ref.[8]	pH 1.5, K_2SO_4 and H_2SO_4		81.0	0.49	12 h	/

Supplementary Table 8. FE values of main products on TCo-CuO NS catalysts under 0.2-1.2 A cm^{-2}. The flow rate of CO_2 inlet was 50 sccm. Values are means, and error bars indicate SD (at least 3 replicates).

j (A cm^{-2})	**$FE_{ethylene}$ (%)**	**$FE_{ethanol}$ (%)**	**$FE_{acetate}$ (%)**	**$FE_{n\text{-}propanol}$ (%)**	**$FE_{hydrogen}$ (%)**
0.2	21.19 ± 1.21	6.67 ± 0.65	0.76 ± 0.47	3.16 ± 0.81	7.21 ± 0.75
0.4	42.4 ± 2.06	9.66 ± 2.13	0.6 ± 0.23	4.68 ± 0.3	8.93 ± 0.4
0.6	52.05 ± 3.62	14.75 ± 0.83	0.72 ± 0.45	5.79 ± 0.93	8.04 ± 0.19
0.8	57.26 ± 1.96	17.8 ± 1.28	1.14 ± 0.06	4.77 ± 1.16	6.6 ± 0.98
1	66.43 ± 3.51	17.88 ± 0.46	1.68 ± 0.23	3.48 ± 1.3	7.45 ± 0.68
1.2	61.2 ± 3.11	18.92 ± 1.12	2.53 ± 0.99	3.74 ± 1.64	10.05 ± 1.71

Reference

1. Xie, Y. et al. High carbon utilization in CO_2 reduction to multi-carbon products in acidic media. Nat. Catal. 5, 564–570 (2022).
2. Tan, Z. et al. Polymeric ionic liquid promotes acidic electrocatalytic CO_2 conversion to multicarbon products with ampere level current on Cu. Nat. Commun. 16, 1843 (2025).
3. Chen, Y. et al. Efficient multicarbon formation in acidic CO_2 reduction via tandem electrocatalysis. Nat. Nanotechnol. 19, 311–318 (2024).
4. Zhao, Y. et al. Conversion of CO_2 to multicarbon products in strong acid by controlling the catalyst microenvironment. Nat. Synth. 2, 403–412 (2023).
5. Fan, M. et al. Cationic-group-functionalized electrocatalysts enable stable acidic CO_2 electrolysis. Nat. Catal. 6, 763–772 (2023).
6. Huang, J. E. et al. CO_2 electrolysis to multicarbon products in strong acid. Science 372, 1074–1078 (2021).
7. Wang, R. et al. Switching the Symmetry of a Trinuclear Copper Cluster Catalyst for Electroreducing CO_2 to an Asymmetric C_2 Product in an Acidic Electrolyte. ACS Catal. 14, 741–750 (2024).

8. Su, L. et al. Multifunction al Conductive Polymer Modification for Efficient CO_2 Electroreduction in Acidic Electrolyte. Adv. Funct. Mater. https://doi.org/10.1002/adfm.202425636 (2025).